A PERSPECTIVE ON THE NUMERICAL AND EXPERIMENTAL CHARACTERISTICS OF MULTI-MODE DRY-FRICTION WHIP AND WHIRL

A Thesis

by

JASON CHRISTOPHER WILKES

Submitted to the Office of Graduate Studies of
Texas A&M University
in partial fulfillment of the requirements for the degree of

MASTER OF SCIENCE

August 2008

Major Subject: Mechanical Engineering

A PERSPECTIVE ON THE NUMERICAL AND EXPERIMENTAL CHARACTERISTICS OF MULTI-MODE DRY-FRICTION WHIP AND WHIRL

A Thesis

by

JASON CHRISTOPHER WILKES

Submitted to the Office of Graduate Studies of
Texas A&M University
in partial fulfillment of the requirements for the degree of

MASTER OF SCIENCE

Approved by:

Chair of Committee,	Dara W. Childs
Committee Members,	Paul Cizmas
	Alan Palazzolo
Head of Department,	Dennis O'Neal

August 2008

Major Subject: Mechanical Engineering

ABSTRACT

A Perspective on the Numerical and Experimental Characteristics of Multi-Mode
Dry-Friction Whip and Whirl. (August 2008)
Jason Christopher Wilkes, B.S., Texas A&M University
Chair of Advisory Committee: Dr. Dara W. Childs

The present work investigates the nature of dry-friction whip and whirl through experimental and numerical methods. Efforts of the author, Dyck, Pavalek, and coworkers enabled the design and construction of a test rig that demonstrated and recorded accurately the character of multi-mode dry-friction whip and whirl. These tests examined steady state whip and whirl characteristics for a variety of rub materials and clearances. Results provided by the test rig are unparalleled in quality and nature to those seen in literature and possess several unique characteristics that are presented and discussed.

A simulation model is constructed using the Texas A&M University (TAMU) Turbomachinery Laboratory rotordynamic software suite XLTRC^2 comprised of tapered Timoshenko beam finite elements to form multiple degree of freedom rotor and stator models. These models are reduced by component mode synthesis to discard high-frequency modes while retaining physical coordinates at locations for nonlinear interactions. The interaction at the rub surface is modeled using a nonlinear Hunt and Crossley contact model with coulomb friction. Dry-friction simulations are performed for specific test cases and compared against experimental data to determine the validity of the model. These comparisons are favorable, capturing accurately the nature of dry-friction whirl.

Experimental and numerical analysis reveals the existence of multiple whirl and whip regions spanning the entire range of frequencies excited during whirl, despite claims of previous investigations that these regions are predicted by Black's whirl solution, but are not excited in simulations or experiments. In addition, spectral analysis illustrates the presence of harmonic sidebands that accompany the fundamental whirl solution. These sidebands are more evident in whip, and can excite higher-frequency whirl solutions. Experimental evidence also shows a strong nonlinearity present in the whirl frequency ratio, which is greater than that predicted by the measured radius-to-clearance ratio at the rub location. Results include whirl frequencies 250% of that predicted by the measured radius-to-clearance ratio.

DEDICATION

To My Parents,
My Wife Monica,
And ________ (in the oven).

ACKNOWLEDGEMENTS

For the experience, knowledge, and humility which were cultivated through the digressions of mind, body, and will in accomplishing this feat, I am grateful to the following individuals: To Monica, my wife, your support and understanding has turned possibility into reality. Dr. Childs, for aiding the brilliance and idiocy that comes with youth, I am indebted, and prey you find compensation in my report. I would also like to thank Northrop Grumman Space Technology, Redondo Beach, CA and Air Force Research Laboratory, Propulsion Directorate, Edwards Air Force Base, CA for the opportunity to partake in what will hopefully become the technology, and inspiration, for future generations. To Steven Phillips, Dustin Pavalek, B. J. Dyck, and Henry Borchard, I praise all of you for your efforts in the design and construction of a phenomenal test rig. To Eddie Denk, I assert that you are the foundation upon which we build our research, our accomplishments, and most of all the cells for better bearings in our life.

TABLE OF CONTENTS

Page

ABSTRACT iii

DEDICATION v

ACKNOWLEDGEMENTS vi

TABLE OF CONTENTS vii

LIST OF TABLES ix

LIST OF FIGURES x

CHAPTER

I INTRODUCTION 1

Literature Review 2
Events Leading Toward Dry-Friction Investigations at TAMU 7
Objective of the Research 9
Method of Investigation 9

II MATHEMATICAL MODEL 10

III TAMU DRY-FRICTION WHIP AND WHIRL TEST RIG 17

General Description 17
Test Rotor 18
Base of Test Stand and Rotor Support 20
Rotor Drivetrain 21
Instrumentation 23
Test Series and Data Analysis 23

IV SIMULATION MODEL 25

Overview of XLTRC^2 Rotordynamics Software Package 25
General System Model 25
Support Asymmetry 26
Vibration Characteristics 26
Nonlinear Connection 28
Simulation Procedure and Post Processing of Data 29
Simulated Bearing Configurations 29

CHAPTER Page

V RESULTS 31

Experimental Dry-friction Whip and Whirl Characteristics 31
Fundamental Observations on the Nature of Dry-Friction Whip and Whirl 31
Presence of Harmonic Sidebands Accompanying Primary Backward Component 33
Absolute and Relative Magnitudes Captured by Proximity Probes 34
Predicted versus Measured Precession-Frequency Ratio (PFR) 38
Existence and Excitation of Multiple Whirl Solutions 42
Simulation Validation 47
Whip and Whirl Frequencies 48
Amplitude Comparison 49
Nature of Frequency Spectrum 51

VI CONCLUSION 53

Experimental Achievements 53
On the Nature of Multi-Mode Dry-Friction Whip and Whirl 53
On the Validity of the Simulation Model 54
Direction for Future Research 55
Development of a More Accurate Rub Model 56
Inclusion of a Sophisticated Structural Model 56

NOMENCLATURE 57

REFERENCES 59

APPENDIX A: CROSS-REFERENCE CHART 63

APPENDIX B: TEST CASE MATRIX 64

VITA 65

LIST OF TABLES

Page

Table 1 Properties of rotor and stator pairs at the rub location 19
Table 2 First horizontal and vertical natural frequencies of the support and test pedestals 21
Table 3 Individual and combined vibration modes for the simulation model 27
Table 4 Nonlinear stiffness and damping coefficients employed in simulations.......... 28
Table 5 Bearing parameters used in simulations.. 29

LIST OF FIGURES

Page

Figure 1 Geometric model governing rotor-stator contact 10
Figure 2 Rotor-stator interaction model, after [26] 11
Figure 3 Individual and combined rotor and stator receptances defining regions in which rotor stator interaction is possible 14
Figure 4 General case of the U-shaped plot attributed to Black.................................... 15
Figure 5 Multi-mode dry-friction whirl prediction for Bartha's test rig [26]................ 16
Figure 6 Picture of TAMU Whip and Whirl Test Rig.. 17
Figure 7 Section View of TAMU Whip and Whirl Test Rig 17
Figure 8 Section view of TAMU Whip and Whirl Test Rig rotor 19
Figure 9 Test base supported on vibration isolators to reduce base natural frequency and orthotropy 20
Figure 10 Drive system comprised of (left to right) coupling , gear reducer, and motor. 22
Figure 11 XLTRC^2 simulation model for TAMU Whip and Whirl Rig 26
Figure 12 Measured (a) frequency and (b) amplitude of max backward whirl component at probe 1 32
Figure 13 Two-sided FFT of probe measurements for typical case of dry-friction whip and whirl 32
Figure 14 FFT of probe 1 measurements in whip at a) 120 rpm and b) 230 rpm rotational speeds... 34
Figure 15 Measured backward precession amplitude versus speed 35
Figure 16 Measured backward precession amplitude relative to probe 1 versus speed... 36
Figure 17 Measured and predicted relative mode shapes for Case 20 at a) 130 rpm and b) 235 rpm 37
Figure 18 Measured probe and accelerometer orbits for Case 20 in a) the first whirl region, b) the first whip region, c) the third whirl region, and d) the third whip region 38
Figure 19 Measured precession frequency ratio versus rotor speed for large clearance bearing... 39

Page
Figure 20 Measured precession frequency ratio versus rotor speed for small clearance bearing 40
Figure 21 Measured precession frequency ratio for Babbitt bearing illustrating rapid increases at low speeds 40
Figure 22 Increase in measured precession frequency ratio toward the end of test Case 3 41
Figure 23 Decrease in measured precession frequency ratio toward the end of test Case 13 42
Figure 24 Measured backward precession frequency versus rotor speed at probe set 1 .. 43
Figure 25 Spectrogram plot showing excitation of higher whirl modes by sideband harmonics 44
Figure 26 FFT at (a) 137.5, (b) 142.5, and (c) 147.5, showing harmonic sideband excitation of a higher whirl mode 45
Figure 27 Physical orbits captured by probes during whip showing unsteady characteristics 46
Figure 28 First whip mode for Babbitt bearing prevalent over higher modes 47
Figure 29 Comparison of measured and predicted backward precession frequencies 48
Figure 30 Predicted backward precession amplitude versus speed for all probes 49
Figure 31 Predicted backward precession amplitude relative to probe 1 versus speed for all probes 50
Figure 32 Predicted and measured backward precession amplitude relative to probe 1 versus speed 51
Figure 33 Frequency spectra for simulation 2 at probe 1 52

CHAPTER I

INTRODUCTION

In the pursuit of efficient operation, manufacturers have tightened clearances in turbomachinery to the extent that rubbing between a rotor and stator is not uncommon. Whether rubbing across an axial or circumferential clearance, a plethora of rub related vibration phenomena exist that can threaten machine integrity. In most cases, rubbing results in the gradual wear and degradation of mating surfaces and requires premature repair or replacement of damaged components. This type of rub is classified as light rub, and is often tolerable. In other instances, rubbing can produce dangerous and possibly catastrophic vibration amplitudes. Heavy rub, as it is termed, can be detrimental to the machine and its surrounding environment. Rub is further categorized into partial or full annular rub, depending on the portion of the whirl orbit in which the rotor remains in contact with the stator. Partial rub occurs between the rotor and stator along a portion of the total whirl arc and is characterized by intermittent contact between the two bodies, whereas full annular rub is characterized by near continuous contact throughout the entire whirl orbit. One of the most destructive rubbing phenomena occurs when a rotor, upon contact with stator across a radial clearance, is forced by traction into a backward precessional orbit. This motion will be classified into the following two regimes for the remainder of this work:

- Dry-friction whirl in which the rotor is rolling-without-slipping on the surface of the stator with a backward precession frequency governed by the radius-to-clearance ratio at the contact location.
- Dry-friction whip in which the rotor slips continuously on the surface of the stator with a backward precession frequency governed by a combined natural frequency of the connected rotor-stator system.

While rub is a serious and costly element in the maintenance of turbomachinery, dry-friction whip and whirl have only been reported a handful of times in industrial failures.

This thesis follows the style of ASME Journal of Vibration and Acoustics.

Though scarce, these failures are serious in nature and should be avoided at all cost. Rosenblum [1] provided several documented incidents of dry-friction whip and whirl in rotating machinery, one of which details the obliteration of a 600 MW turbo generator in 1972. The instability began in the low pressure turbine and progressed to the high pressure turbine, which sheared in 16 places due to the excessive torques and alternating stresses present during the event. Though rare, an instance of dry-friction whip and whirl is a highly destructive and complicated rub event that must be respected in the design of turbomachinery.

LITERATURE REVIEW

In 1926, Newkirk [2] was investigating shaft rubbing when, upon a sufficiently hard contact with the stator, the shaft began to whirl violently counter to the direction of rotation. Though he did not go on to investigate the instability, Newkirk was the first to recognize and document dry-friction whip or whirl. The next efforts on the subject were those of Baker [3] and Den Hartog [4], who established the principles of reverse whirl from an intuitive perspective. Using a simple geometrical model of the rotor-stator contact plane, Baker and Den Hartog derived the kinematic constraint relating the whirl frequency to shaft speed as the radius-to-clearance ratio resulting from the assumption of no-slip at the contact location.

In 1962, Johnson [5] investigated the synchronous whirling characteristics for a shaft having a clearance in one bearing. Though he did not investigate the possibility of reverse whirl, he established a framework that is fundamental to the analysis of rotor-stator interaction. In regard to the legitimacy of solutions describing the motion of a rotor and stator having contact, Johnson states that "the following must be examined:

(a) Whether the solutions are real.
(b) Whether the reaction between the clearance bearing and the shaft is positive (in compression).
(c) Whether the equilibrium is stable so that any small oscillations which the shaft may have, about that equilibrium position, are damped." [5, pp. 90]

The first in-depth investigation on the friction-induced instability was Billett [6], who in 1965 used a Jeffcott style rotor having a clearance at the bearing to illustrate the fundamental aspects of dry-friction whip and whirl. Billett proposed that the occurrence of slip between the rotor and stator explained why shafts whirled close to their natural frequency throughout a wide range of running speeds. He showed that regardless of friction coefficient, the simple model cannot whirl faster than its first natural frequency without pulling away from the stator. In addition, Billett solved for the friction coefficient that is required to sustain steady reverse whirl. This can be used to determine the whirl frequency at which the friction coefficient needed to sustain steady whirling is greater than the rotor-stator coulomb friction coefficient, thus resulting in a transition to whip. Billett experimentally produced dry-friction whip and whirl on his simple rotor using three different clearance ratios, all of which transitioned to whip just below the natural frequency of the rotor. Though his model was simple, Billett's analysis explained the reason for near-resonant whirl over a large range of shaft speeds and showed analytically the importance of the friction coefficient and damping in determining the possibility of dry-friction whirl.

The next developments in dry-friction whip and whirl were made by Black [7,8] in 1967 and 1968, who extended the methods employed by Johnson and Billett to include contact with a compliantly mounted stator. Black developed a general model for synchronous rubbing and reduced it to investigate dry-friction counterwhirl. He performed analysis and experimental verification on a Jeffcott rotor contacting a compliant stator at mid-span, which coincided with the mass center of the rotor and stator. Black represented the rotor and stator properties using receptances, assuming both can be regarded as linear multi-degree of freedom systems in which the individual modal properties are known. Black concluded that dry-friction whirl is only possible in the frequency band extending from an individual rotor/stator natural frequency to the next higher combined system natural frequency. This range is further reduced by the condition placed on the traction angle, which Black resolved into a plot having a characteristic U-shape, which differentiates between regions of whirl and whip. Black validated his dry-friction whip and whirl predictions using a test rig that used a loose ball bearing in place of a solid rub surface to reduce drive torques.

To ascertain general guidelines for the avoidance of dry-friction whip, Ehrich [9] performed a parametric study on a simple overhung disk in 1969. In contrast to Black who determined the steady state characteristics of whirl, Ehrich's motivation was to provide those in industry with a rule of thumb to avoid dry-friction instabilities. Ehrich concluded that rotor and stator damping should be similar, while their natural frequencies dissimilar. Ehrich was also the first to perform dry-friction whip and whirl tests on rotor-stator interaction having a realistic radius-to-clearance ratio.

In 1987, Choy and Padovan [10] investigated dry-friction whip and whirl through the numerical integration of the nonlinear equations of motion. They neglected the mass of the stator and modeled the contact using a linear stiffness; however, they produced simulations that showed the inclusion of bounce modes, contact initiation, and steady state behavior.

One year later, Zhang [11] demonstrated the need to account for multiple rotor modes in dry-friction whip and whirl by applying Black's model to a long-cantilevered disk. Zhang identified the same unstable regions as Black, asserting the validity of Black's results by confirming that the dry-friction whirl can exist for all ranges between a rotor natural frequency and the next higher natural frequency of the rotor-stator system pinned together at the contact location. In addition, Zhang presented a condition for the critical contact velocity required to initiate dry-friction whirl.

In 1990, Lingener [12] and Crandall [13] revisited the analytical and experimental work of Black [8] by applying it to a test rig that could be adapted to test several different combinations of rotor and stator properties. Their test rotor had axially shiftable masses on either side of the rub surface and a variable stiffness stator. The analysis presented by Lingener and Crandall indicated that Black's model was found to be generally valid in predicting whirl ranges. Lingener concludes that "it is impossible, to run through any resonance of the joined system, excited by reverse whirl" [12, pp.18], despite this prediction using Black's model. This feat has been accomplished recently by Choi [14] and Dyck [15]. Black [8] presented the possibility of returning to whirl after traveling through a whip region; however, he indicated that vibration modes having a node at the rub location cannot be excited. The majority of tests performed by Lingener and Crandall suggest that the second bending mode would not be excited. Thus, speeds approaching the third bending mode would be required to reinstate whirl above the initial whip region. In addition to extensively validating Black's whip and whirl model, Crandall and Lingener performed tests on an asymmetric system to determine its effect on dry-friction whip and whirl. Results indicated an elliptical orbit and a slight suppression of dry-friction instabilities. These conclusions were supported by Ghauri et al. [16] who simulated dry-friction whip and whirl in an asymmetric stator. The simulations were performed using a validated finite element code with contact modeled by Coulomb friction and a coefficient-of-restitution. In general, Ghauri et al. were interested in the response ensuing from the large imbalance created by a blade loss and its capacity to initiate dry-friction whip and whirl. Other efforts concerning dry-friction due to imbalance include those by Faterella [17], Bartha [18,19], Yu et al. [20], and Cole and Keogh [21]. Experimental work by Yu et al. demonstrated dry-friction whirl and whip initiated upon contact and following synchronous full annular rub while traversing a critical speed. The events occurred with ascending and descending speed.

In the 1990's, interest in dry-friction whip and whirl was motivated by concern in other industries. With advances in oilwell drilling technology, Jansen [22] and Chen [23] applied the principles of dry-friction whip and whirl to downhole drillstring vibrations by investigating the interaction of drill collar stabilizers with the casing through numerical and experimental approaches. In the bearing industry, increasing popularity of the active magnetic bearing (AMB) led to several publications concerning rotor-stator contact interaction following the failure of an AMB. In general, these works address matters concerning the prevention and initiation of dry-friction instabilities. Fumagalli [24] designed a well instrumented test rig consisting of an AMB-supported short rigid rotor that uncoupled from the drive shaft when dropped on a rigid stator. Fumagalli carefully measured power loss and contact force during the dry-friction instability, recording forces upwards of 5500 lb (24.5 kN) for a 7 lb (3.2 kg) rotor. In addition, Fumagalli implemented a nonlinear Hunt and Crossley [25] contact model to characterize rotor-stator interaction in numerical simulations. This implementation was popular for subsequent research, having been applied by Bartha [18,19], Childs and Bhattacharya [26], Popprath and Ecker [27], the author, and others. Fumagalli also performed tests on a variety of rub surfaces to characterize the influence of friction coefficient, compliance, and material compatibility. Later work investigating the effect of different stator materials, Yu et al. [20], Choi [14], and Dyck [15] support conclusions that the friction coefficient is the fundamental parameter of concern; however, Yu et al. and Dyck caution against the use of Babbitt-coated stators, having witnessed rapid and complete deterioration of the engineered surfaces.

Following closely the interests of Fumagalli, Bartha [18, 19] produced a wealth of knowledge on the subject of dry-friction whip and whirl. Bartha's work stemmed from the capability of his test rig to produce accurate excitation schemes using a high power AMB. Bartha validated the critical impact velocity given by Zhang [11] following extensive tests having a variety of impact angles and velocities. Although Bartha noted that impacts having a backward tangential velocity component were more likely to initiate dry-friction whirl, he concluded that the normal impact velocity was the predominant influence. These results were paralleled by numerical simulations using experimentally determined parameters in Hunt and Crossley's [25] vibro-impact model. Bartha addressed several questions concerning the stability of whirl motions in numerical simulations and experiments. He concluded that numerical simulations were unstable without accounting for the relative surface velocity at the contact location. Introducing this effect into the rub model resulted in a slow periodic fluctuation of the relative contact velocity during numerical simulations that introduced harmonic multiples into the frequency spectrum. These multiples occur at a frequency slightly more than twice the main backward component, which Bartha described as closely resembling the motion of a system having stick-slip behavior. In addition Bartha cites a lack of congruence between whirl ranges predicted using Black's dry-friction counterwhirl model and those achieved experimentally.

In 2002, Choi [14] succeeded in traversing through a whip region for a test rig closely resembling the test rig of Lingener [12] and Crandall [13]. Using Black's model, Choi verified the friction-dependent transition frequencies for aluminum and acryl stators. He also mentions the presence of super-harmonic and sub-harmonic frequencies present in the frequency spectrum.

In 2007—following implications by Bartha [18, 19] and Yu et al. [20] that application of Black's whirl model to experimental apparatus predicted erroneous whirl ranges—Childs and Bhattacharya [26] revisited the work of Black to reassert the viability of his dry-friction counterwhirl model. Childs and Bhattacharya state the following: (1) The ability to predict accurate whirl ranges requires the development of an accurate rotor-stator model. This may require the use of multiple rotor/stator modes, as needed to model the test rigs of Bartha and Yu et al. This necessity was mentioned by Black and Zhang [11]; however, Black did not extend his method to multi-mode rotor-stator interaction, and Zhang failed to produce multiple whirl regions. (2) Employing a multi-mode rotor-stator model results in several U-shaped curves, thus predicting several possible whirl regions. Though predicted, only the first whirl range and corresponding whip frequency could be produced in simulations.

Recently, investigations on the initiation of dry-friction whip and whirl have shifted to nonlinear analysis techniques. On the nonlinear nature of full-annular reverse whirl, Williams [28,29] analytically and experimentally investigated the existence of limit cycles during established dry-friction whirl. Williams concluded that although the initiation of dry-friction whip and whirl may be more likely for a system having tighter clearances, the nature of the limit cycle is preferable to one with large clearances. The larger portion of nonlinear investigations has been the study rotor-stator interaction involving periodic contact modes. Researchers on this subject include Neilson and Barr [30], Tamura et al. [31], Cole and Koegh [32,21], and Popprath and Ecker [27]. Both Cole and Keogh, and Popprath and Ecker presented methods by which decomposition of the contact and ensuing vibration leads to the existence of solutions involving intermittent periodic contact between the rotor and stator. Cole and Keogh focused more on the effect of imbalance on the systems bounce modes, whereas Popprath and Ecker focused on the development of a more generalized approach to modeling contact. Both papers compared analytical predictions to the experimental results presented by Tamura et al. and found comparisons favorable.

EVENTS LEADING TOWARD DRY-FRICTION INVESTIGATIONS AT TAMU

In 1995 the U.S. Air Force, Army, Navy, and NASA implemented a 15-year rocket propulsion technology improvement program with the goal of “doubling rocket propulsion technology". This goal would be accomplished by advancing component technology to yield greater performance, reliability, and reduced weight. The U. S. Air Force Research Laboratory (AFRL), Space and Missile Propulsion Division, Edwards AFB, CA, committed to develop an Advanced Liquid Hydrogen (ALH) Turbopump that would approach these objectives through the implementation of fluid-film bearings in place of conventional rolling element bearings. This change was predicted to increase reliability and accommodate higher speeds, which allows an overall reduction in size and weight. To accomplish this, AFRL commissioned Pratt & Whitney (P&W) Liquid Space Propulsion to design and build the ALH. The design by P&W features a single piece rotor with unshrouded impellers to be supported by hydrostatic journal bearings and a single hydrostatic thrust bearing. The hydrostatic bearings are supplied by the pump discharge, which results in little or no rotor support during low speed operation.

In 1998, the ALH was ready for testing at P&W's high-pressure cryogenic test facility. From 1998 through 2002, 20 tests were performed on 11 different builds of the ALH; only the first of these ran according to plan. Following test 1, the development of large supersynchronous vibrations at low speeds overpowered the drive capabilities of the turbopump and halted the rotor. Hardware inspection showed visual signs of rubbing at several locations, specifically the surfaces of the radial and thrust bearings [33].

In the end, the ALH turbopump failed to meet the desired objectives. Learning from the development of the ALH, AFRL acquired the services of Northrop Grumman Space Technology (NGST), through a competitive acquisition, to continue with the Upper Stage Engine Technology (USET) Program, which strives to enhance the efficient design, development, and testing of a liquid rocket propulsion turbopump. To accomplish these goals, USET focused on the improvement and validation of component design, modeling, and simulation tools.

In 2004 NGST contacted the Texas A&M Turbomachinery Laboratory regarding the low speed instability encountered during the ALH startup. In response, Childs [34] raised several questions regarding the transient operation of hydrostatic bearings supplied by gaseous hydrogen. He mentioned the following possible consequences resulting from unsteady supply pressure:

- Limited load capacity.

- Pneumatic hammer.
- Choking of the flow through the bearing orifices (San Andres).

Childs proposed that dry-friction whip and whirl resulting from low bearing stiffness and forced rotor-stator contact were likely the cause of the severe vibrations encountered in the ALH. The result of these deliberations was the commissioning of a test rig to examine the nature of dry-friction whip and whirl in the ALH, and ultimately provide a benchmark test result on which the capability of dry-friction simulation methods could be established. The experimental and numerical exploration of this test rig provides the focal point for the investigations present in this thesis.

OBJECTIVE OF THE RESEARCH

The first objective of this thesis is to investigate the nature of dry-friction whip and whirl with the experimental data obtained on the TAMU Dry-Friction Whip and Whirl Test Rig. The second objective is to develop a model using XLTRC^2 that reliably simulates the observed whip and whirl behavior. This objective is accomplished by comparing the speed-dependent frequency and amplitude characteristics of the experimental and numerical results.

METHOD OF INVESTIGATION

Analysis will begin by investigating the fundamental theories on dry-friction whip and whirl. Following a basic understanding of the subject, the layout of the test rig will be presented to enable the reader to become familiar with the system to be modeled and assumptions required to fully parametrize the model; this will flow into a description of the numerical model that was determined for the test rig and its predicted whirl regions. The thesis will conclude by presenting experimental dry-friction whip and whirl results and how they compare to numerical simulations.

CHAPTER II

MATHEMATICAL MODEL

Using a model similar to the one given in Figure 1, Baker [3] and Den Hartog [4] proposed the following.

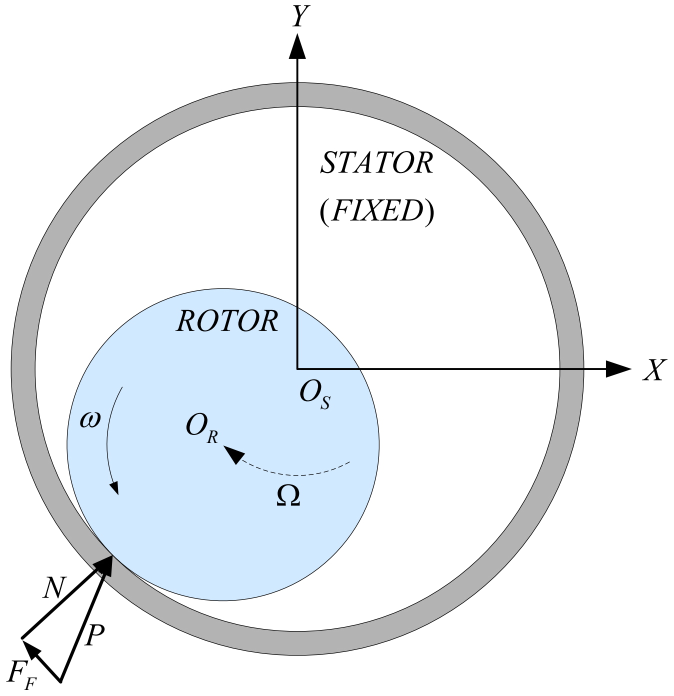

Figure 1 Geometric model governing rotor-stator contact

Upon contact with the stator, a spinning rotor would be acted upon by a normal force N and tangential force $F_F = \mu_d N$, where μ_d represents the dynamic coefficient of friction between the contacting surfaces. Representing the tangential force as a force acting through the rotor's center O_R and a couple about O_R, the rotor will be driven in a clockwise direction about the center of the stator O_S with angular velocity Ω at the expense of an increase in drive torque. Provided the normal force and coefficient of friction are sufficiently large to prevent a steady slipping condition, the rotor will eventually roll on the surface of the stator such that a kinematic constraint exists between the angular velocities of the rotor and its whirl orbit. This constraint is given by

$$\Omega = \tfrac{R}{C_r}\,\omega = \Gamma\omega\,, \tag{1}$$

where Γ, the precession frequency ratio (PFR), represents the ratio of whirl frequency to shaft speed that is governed by the measured radius-to-clearance ratio at the contact location. In a realistic turbomachine the clearance is usually 100 to 1000 times smaller than the radius; therefore, dry-friction instabilities at low speeds can still produce high-frequency vibrations. Proceeding along the intuitive line of thought started above, one can see that when the rotor is rolling without slipping on the surface of the stator, the friction force is not governed by the available coulomb friction coefficient (μ_d), but by the force necessary to sustain the rotors whirl orbit. This is referred to as the required friction coefficient (μ).

Having established an intuitive understanding of the basic principle of dry-friction whip and whirl, a more rigorous mathematical model is to be derived. The analytical method presented here follows that originally proposed by Billett [6] and Black [8], with refinements provided by Zhang [11], and most recently Childs and Bhattacharya [26]. Proceeding with the assumption that the rotor and stator can be regarded as known linear multi-degree of freedom systems as indicated by Black [8], our derivation begins with the simple case of a two degree-of-freedom rotor and stator shown at the plane of contact in Figure 2.

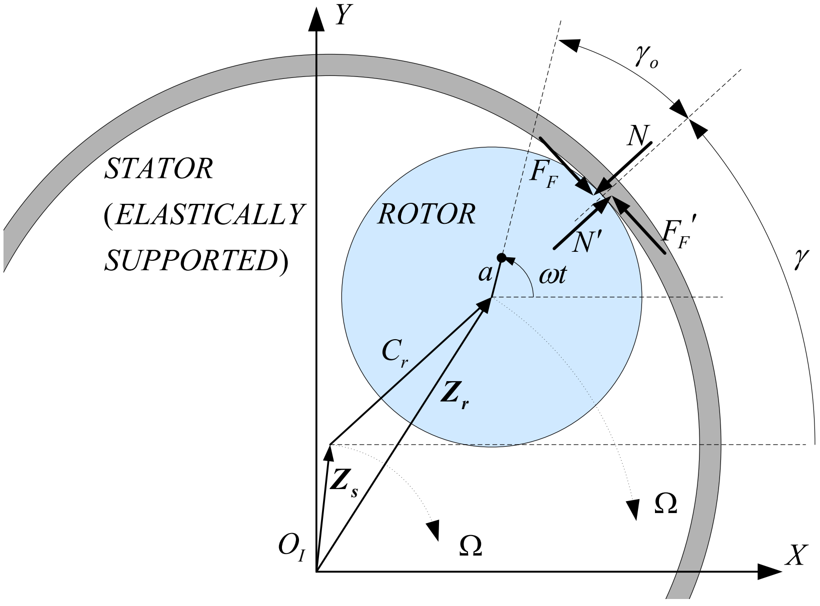

Figure 2 Rotor-stator interaction model, after [26]

Using $\boldsymbol{Z_r}$ and $\boldsymbol{Z_s}$ to denote the complex rotor and stator displacements ($\boldsymbol{Z_r} = \mathrm{X}_r + j\,Y_r$), the general nonlinear equations of motion are given as

$$\begin{gathered} m_r\ddot{\boldsymbol{Z}}_{\boldsymbol{r}} + c_r\dot{\boldsymbol{Z}}_{\boldsymbol{r}} + k_r\boldsymbol{Z}_{\boldsymbol{r}} = \begin{cases} -\left(N + jF_F\right)e^{j\gamma} + m_r a\omega^2 e^{j\omega t} & \left|\boldsymbol{Z_r} - \boldsymbol{Z_s}\right| = C_r \\ m_r a\omega^2 e^{j\omega t} & \left|\boldsymbol{Z_r} - \boldsymbol{Z_s}\right| < C_r \end{cases} \\ m_s\ddot{\boldsymbol{Z}}_{\boldsymbol{s}} + c_s\dot{\boldsymbol{Z}}_{\boldsymbol{s}} + k_s\boldsymbol{Z}_{\boldsymbol{s}} = \begin{cases} \left(N + jF_F\right)e^{j\gamma} & \left|\boldsymbol{Z_r} - \boldsymbol{Z_s}\right| = C_r \\ 0 & \left|\boldsymbol{Z_r} - \boldsymbol{Z_s}\right| < C_r \end{cases} \end{gathered} . \tag{2}$$

Neglecting the effect of rotor imbalance and limiting the discussion to full annular rub, the equations of motion reduce to

$$\begin{aligned} m_r\ddot{\boldsymbol{Z}}_{\boldsymbol{r}} + c_r\dot{\boldsymbol{Z}}_{\boldsymbol{r}} + k_r\boldsymbol{Z}_{\boldsymbol{r}} &= -\left(N + jF_F\right)e^{j\gamma} \\ m_s\ddot{\boldsymbol{Z}}_{\boldsymbol{s}} + c_s\dot{\boldsymbol{Z}}_{\boldsymbol{s}} + k_s\boldsymbol{Z}_{\boldsymbol{s}} &= \left(N + jF_F\right)e^{j\gamma} \end{aligned} . \tag{3}$$

Since we are interested in the steady state properties of the system, we will seek a periodic solution of the form

$$\boldsymbol{Z_r} = \boldsymbol{z_r}e^{-j\Omega t}, \quad \boldsymbol{Z_s} = \boldsymbol{z_s}e^{-j\Omega t}, \quad \gamma = -\Omega t + \gamma_o \,. \tag{4}$$

Plugging the assumed solution and its derivatives into the equation of motion, one obtains

$$\begin{aligned} \left(k_r - m_r\Omega^2 - j\,c_r\Omega\right)\boldsymbol{z_r}e^{-j\Omega t} &= \frac{\boldsymbol{z_r}e^{-j\Omega t}}{\boldsymbol{\alpha_{11}}(-\Omega)} = -\left(N + jF_F\right)e^{j\gamma} \\ \left(k_s - m_s\Omega^2 - j\,c_s\Omega\right)\boldsymbol{z_s}e^{-j\Omega t} &= \frac{\boldsymbol{z_s}e^{-j\Omega t}}{\boldsymbol{\beta_{11}}(-\Omega)} = \left(N + jF_F\right)e^{-j\gamma} \end{aligned} , \tag{5}$$

where Black introduces rotor and stator receptances $\boldsymbol{\alpha_{11}}(-\Omega)$ and $\boldsymbol{\beta_{11}}(-\Omega)$ to facilitate the solution process. In addition to the individual equations of motion, solution of Eq. (5) requires an additional equation relating the rotor and stator displacements to the clearance vector. This is accomplished by the constraint equation

$$C_r e^{j\gamma} = \boldsymbol{Z_r} - \boldsymbol{Z_s} = \left(\boldsymbol{z_r} - \boldsymbol{z_s}\right)e^{-j\Omega t} \tag{6}$$

which uses the steady state displacement vectors provided by Eq. (5) to obtain

$$C_r e^{j\gamma_o} = \boldsymbol{z_r} - \boldsymbol{z_s} = -\left[\boldsymbol{\alpha_{11}}(-\Omega) + \boldsymbol{\beta_{11}}(-\Omega)\right]\left(N + jF_F\right)e^{j\gamma_o} \,. \tag{7}$$

Eliminating the unnecessary exponents and rearranging terms yields

$$\left(N + jF_F\right) = -C_r\left[\boldsymbol{\alpha_{11}}(-\Omega) + \boldsymbol{\beta_{11}}(-\Omega)\right]^{-1}, \tag{8}$$

which constitutes an algebraic system of equations that define the frequency dependent contact force and traction angle for any known system. Though it is a bit tedious, one may represent the receptances $\boldsymbol{\alpha}_{11}(-\Omega)$ and $\boldsymbol{\beta}_{11}(-\Omega)$ as

$$\begin{aligned}\boldsymbol{\alpha}_{11}(-\Omega) &= \frac{1}{\sigma_\alpha + i\varphi_\alpha} = \frac{\sigma_\alpha - i\varphi_\alpha}{\sigma_\alpha^{\,2} + \varphi_\alpha^{\,2}} = \frac{\sigma_\alpha - i\varphi_\alpha}{D_\alpha} \\ \boldsymbol{\beta}_{11}(-\Omega) &= \frac{1}{\sigma_\beta + i\varphi_\beta} = \frac{\sigma_\beta - i\varphi_\beta}{\sigma_\beta^{\,2} + \varphi_\beta^{\,2}} = \frac{\sigma_\beta - i\varphi_\beta}{D_\beta},\end{aligned} \tag{9}$$

and their sum as

$$\boldsymbol{\alpha}_{11}(-\Omega) + \boldsymbol{\beta}_{11}(-\Omega) = \frac{\left(D_\beta\sigma_\alpha + D_\alpha\sigma_\beta\right) - j\left(D_\alpha\,\varphi_\beta + D_\beta\varphi_\alpha\right)}{D_\alpha D_\beta} = \frac{S_\sigma - j\,S_\varphi}{D_\alpha D_\beta}. \tag{10}$$

Substituting Eq. (10) into Eq. (8) and making the denominator real results in

$$\left(N + jF_F\right) = \frac{-C_r D_\alpha D_\beta}{S_\sigma - j\,S_\varphi} = \frac{-C_r D_\alpha D_\beta\left(S_\sigma + j\,S_\varphi\right)}{S_\sigma^{\,2} + S_\varphi^{\,2}} \tag{11}$$

Though it may seem that Eq. (11) is excessive, the required friction coefficient μ that satisfies the steady state whirl solution can be expressed by the simple relation

$$\mu = \frac{F_F}{N} = \frac{S_\varphi}{S_\sigma}. \tag{12}$$

In addition, the real part of Eq. (11) yields the normal force as

$$N = \frac{C_r D_\alpha D_\beta}{D_\beta\left(\sigma_\alpha + \mu\varphi_\alpha\right) + D_\alpha\left(\sigma_\beta + \mu\varphi_\beta\right)}. \tag{13}$$

Though they are expressed in a different form, these are equivalent to the solutions obtained by Black. While Eq. (8) was solved analytically, Black presents an elegant synopsis of the method through its implication in the absence of damping. Black proposes the following. If rotor-stator interaction is possible, than the right hand side of Eq. (8) is real, thus there can be no friction force. From this result, it can be seen that the normal force given by

$$N = -C_r\left[\boldsymbol{\alpha}_{11}(-\Omega) + \boldsymbol{\beta}_{11}(-\Omega)\right]^{-1} \tag{14}$$

requires that the inequality

$$\left[\boldsymbol{\alpha}_{11}(-\Omega) + \boldsymbol{\beta}_{11}(-\Omega)\right] < 0 \tag{15}$$

must be met if the normal force is to be positive. This condition is illustrated graphically in Figure 3 using the individual and combined receptances of the rotor-stator system.

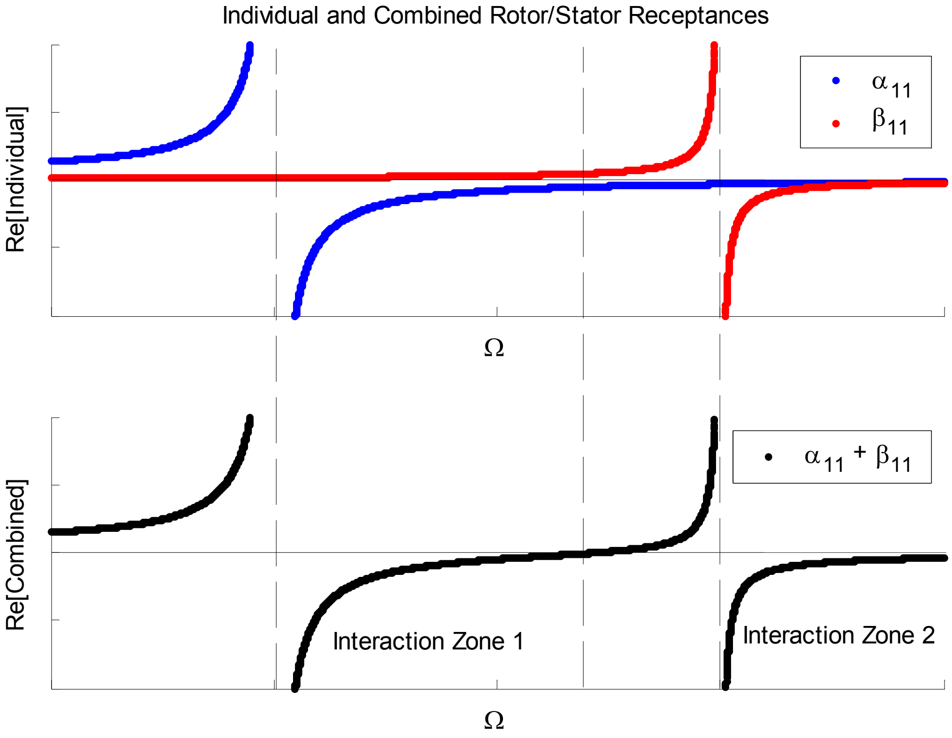

Figure 3 Individual and combined rotor and stator receptances defining regions in which rotor stator interaction is possible

In light of the graphical representation of rotor and stator receptances, the sum of rotor-stator receptances becomes negative when traversing an individual rotor or stator natural frequency, and positive when traversing a combined natural frequency. Combined in this instance denoting that the two are pinned together at the contact location, resulting in

$$\omega_{n,comb} = \sqrt{\frac{k_r + k_s}{m_r + m_s}} \tag{16}$$

for the undamped system considered here. From this, Black illustrates that dry-friction whirl is only possible from an individual rotor/stator natural frequency to its next higher combined system natural frequency. In addition, the frequency range for which dry-friction whirl can occur is further reduced by the condition placed on the necessary traction angle as defined in Eq. (12). From this relation, Black generated a plot having a characteristic U-shape to differentiate between regions of whip and whirl. An example of the U-shaped plot attributed to Black is given for a lightly damped system in Figure 4.

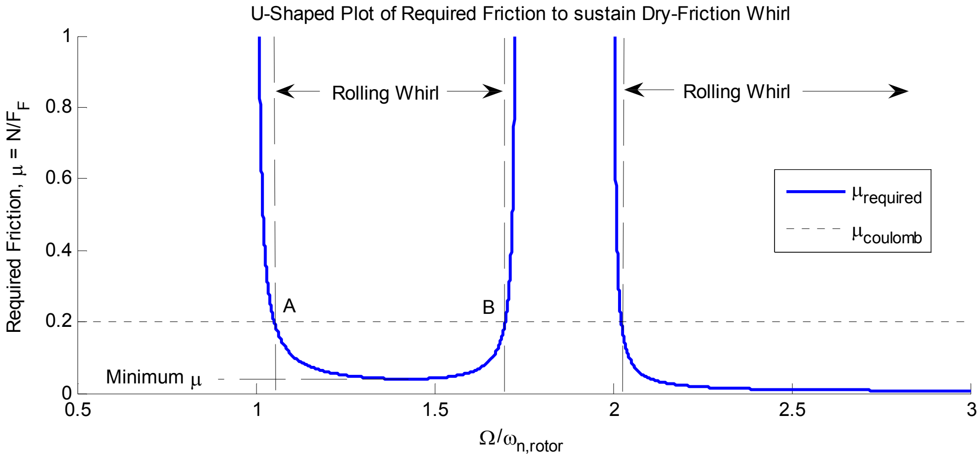

Figure 4 General case of the U-shaped plot attributed to Black

To generate this plot, the required coefficient of friction or traction angle is plotted as a function of whirl frequency, thus establishing the range of frequencies for which the rotor-stator coulomb friction coefficient is sufficient to sustain dry-friction whirl. The left side of the U-shape curve forms a boundary between unstable/ unattainable solutions below and stable/attainable solutions above. From the point of entry denoted A in Figure 4, an increase in shaft speed is accompanied by a reduction of the required traction angle; however, a decrease in speed results in an increase of traction beyond the available value, resulting in subsequent decrease in whirl frequency. Position A is therefore an unstable solution. Position B, on the other hand, separates a stable solution on the left, from an unattainable solution on the right. Thus, a reduction in speed at B results in a decrease in traction required followed by a decrease in whirl frequency; however, an increase in speed would result in a loss of traction and yield steady slip at the frequency governed by B, otherwise known as the whip frequency. Thus for the damped case, the solution at position B could be considered stable. Note that the U-shaped curve provides a minimum traction angle which will sustain whirl. Thus, without adequate coulomb friction, dry-friction whirl can not exist.

Black validated his dry-friction whip and whirl predictions using a Jeffcott rotor rubbing on a ball bearing at the mid-span. Not only did Black present a simple and accurate model that can accurately predict ranges in which whip and whirl can occur, he did so in an elegant and insightful manner.

Extending Black's method for the case of a multi-mode rotor and stator, Childs and Bhattacharya [26] developed plots having several whirl regions. The multi-mode whirl prediction for Bartha's test rig given in Figure 5 illustrates the importance of proper modeling in predicting regions of whip and whirl. Using only one rotor mode to predict whirl, Bartha predicted a transition to whip close to 1600 Hz. After transitioning to whip at 600 Hz, Bartha attributed the discrepancy to a flaw in Black's whirl solution. With proper application, Black's model predicts a transition to whip at 650 Hz, which is close to the measured transition.

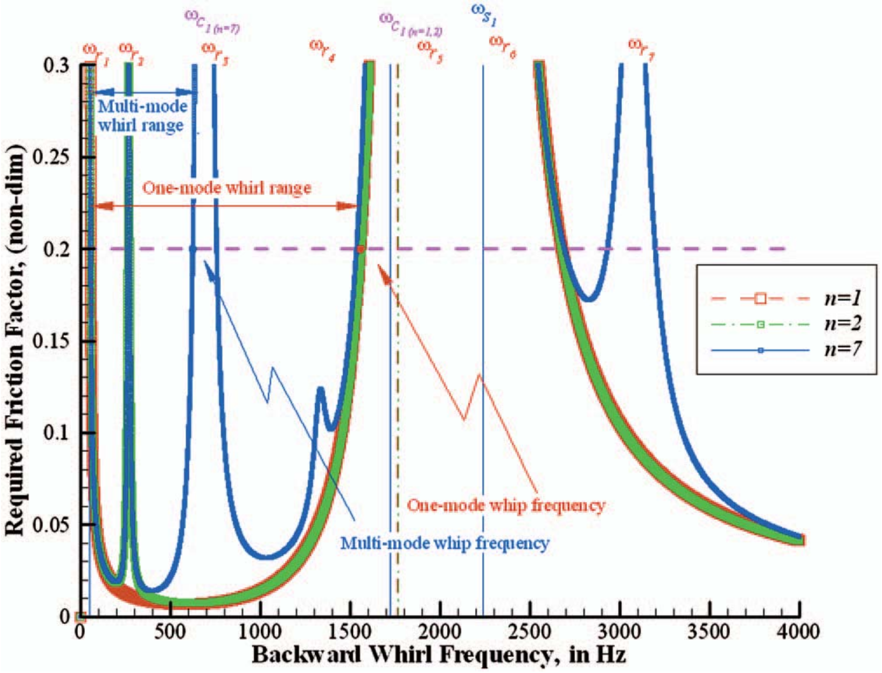

Figure 5 Multi-mode dry-friction whirl prediction for Bartha's test rig [26]

CHAPTER III

TAMU DRY-FRICTION WHIP AND WHIRL TEST RIG

GENERAL DESCRIPTION

A picture of the TAMU Whip and Whirl Test Rig is shown in Figure 6 and a detailed section view of the test rig is given in Figure 7.

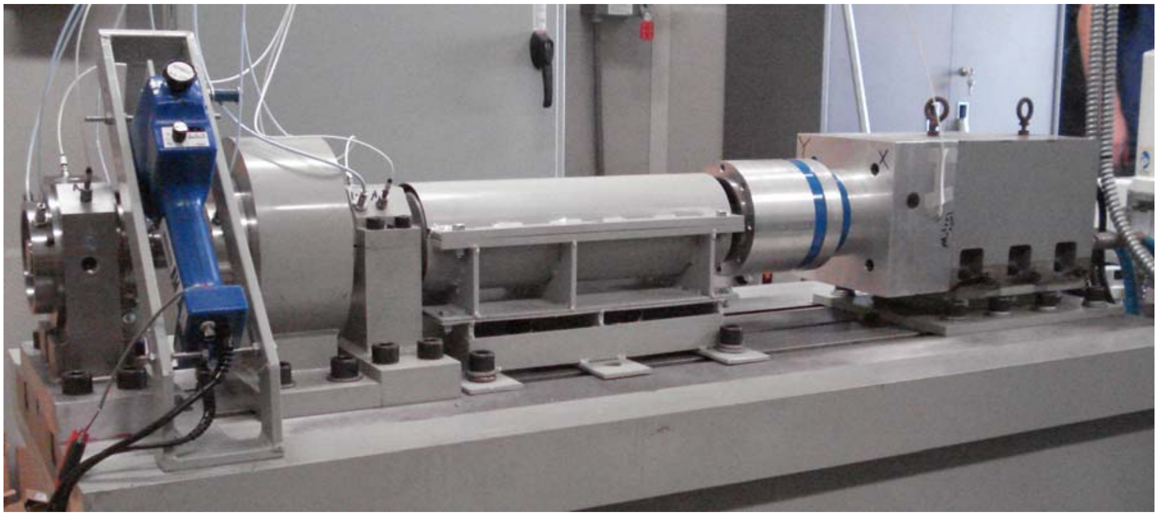

Figure 6 Picture of TAMU Whip and Whirl Test Rig

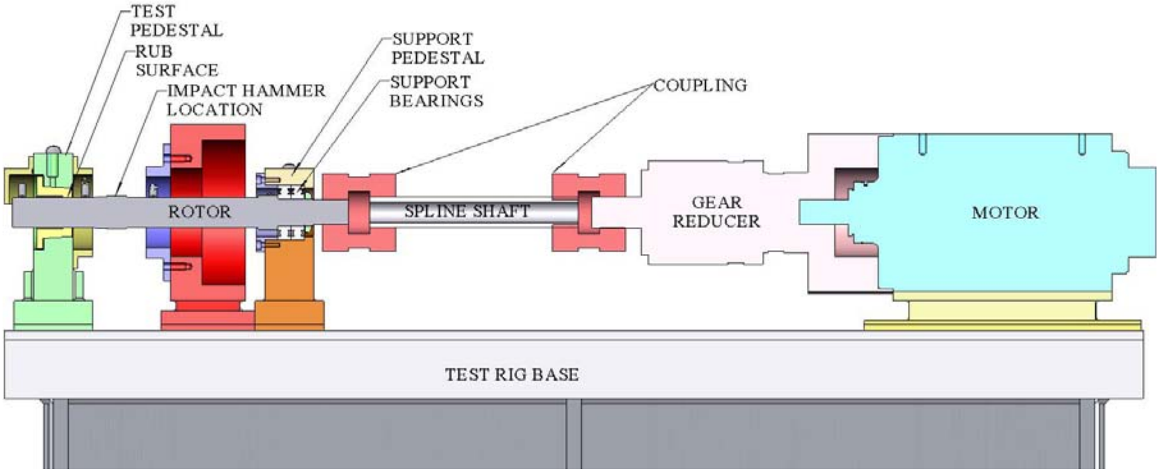

Figure 7 Section View of TAMU Whip and Whirl Test Rig

The section view in Figure 7 shows that the rotor is supported from the right where two adjacent angular contact ball bearings provide a large radial stiffness and little angular support. On the left, the test rotor rubs on an interchangeable rub insert that enables whip and whirl testing for different stator materials and radial clearances. Motion was observed by four pairs of proximity probes located along the shaft in addition to a pair of accelerometers on each pedestal so that different whirl modes could be observed. Contact between the rotor and stator was induced using an impulse hammer located close to the rub surface. Though the force produced by the impact hammer was measured, the initiation of whirl was not the focus of the project and will not be discussed in further detail. Because whip and whirl testing was performed for rotor speeds ranging from 0-250 rpm, the shaft was driven by a high-power motor through a gear reducer to provide high torque at low speeds. The drive system was connected to the test rotor through a spline shaft to minimize the effects of misalignment between the test rotor and drive system. This cannot be seen in the picture because it is hidden by the coupling guard, a precautionary shield installed to contain the couplings and spline-shaft in the event of a failure. These components were all mounted and aligned on a heavy test base attached to the ground through soft springs. These springs prevented the transmission of high frequency vibration loads to the ground; this reduced the influence of base motion on high frequency whip and whirl motion and reduced orthotropy in the base support.

TEST ROTOR

The most important aspect of the test rig is the rotor. Designed to emulate the conditions present in a rocket engine turbopump, the shaft was machined from a solid piece of AISI 4140 steel and has an average diameter of 1.5 in (3.81 cm) and a length of 17.08 in (0.433 m). With these dimensions and ball bearings with stiffness 480,000 $^{\mathrm{lb}}/_{\mathrm{in}}$ (80.6 $^{\mathrm{MN}}/_{\mathrm{m}}$), the lowest three calculated natural frequencies of the shaft are 40.9 Hz, 418.5 Hz, and 810.6 Hz, where 40.9 Hz represents the cantilevered mode, and the next two are the first and second bending modes of the rotor. A closer view of the rotor is given in Figure 8 and provides more detail on the location of probes, accelerometers, and rubbing contact.

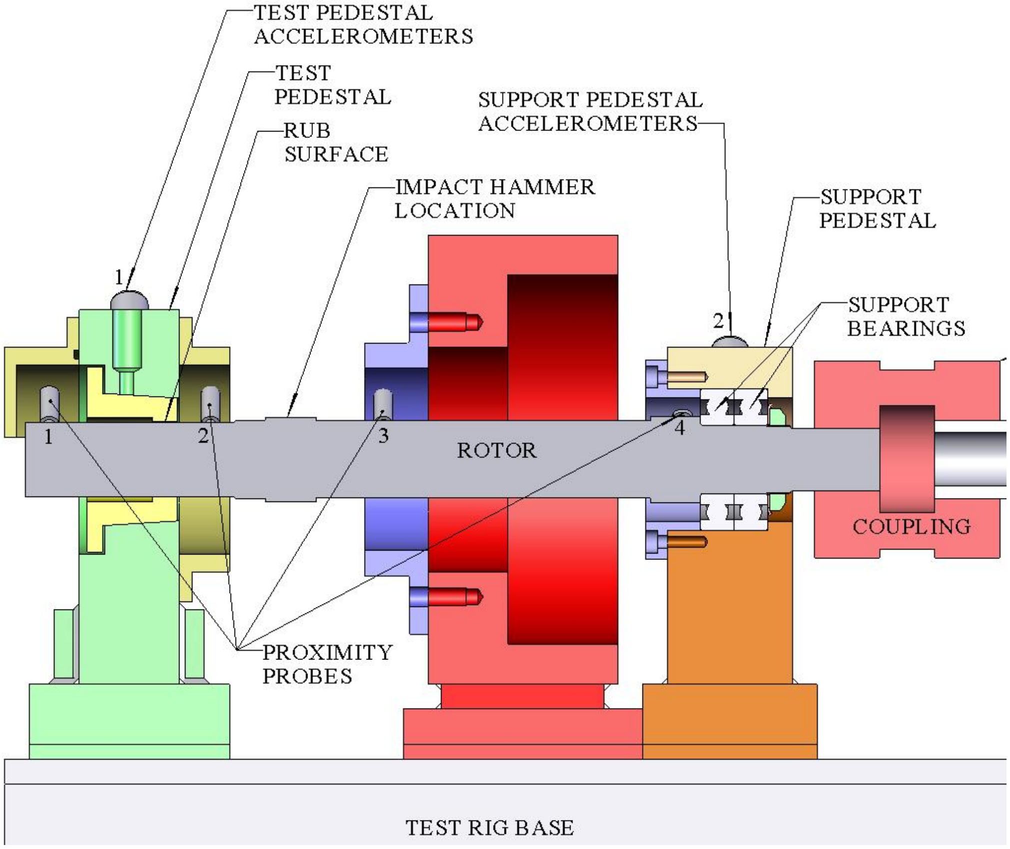

Figure 8 Section view of TAMU Whip and Whirl Test Rig rotor

The rub surface is located approximately 2.79 in (7.087 cm) from the free end of the rotor. At this location, the diameter of the rotor was measured as 1.4997 in (3.809 cm). Four different stator inserts were machined to test the effects of clearance and material on dry-friction whip and whirl motion. These properties are summarized in Table 1 [15].

Table 1 Properties of rotor and stator pairs at the rub location

Designation	Diameter in ± 0.1 mils (cm ± 0.25 μm)	R/C_r	Material	Hardness (HB)	Hardness Ratio	Friction Coefficient [35,36]
Rotor	1.4997 (3.809)	-	AISI 4140	197	-	-
Bearing S1,S2	1.5026 (3.817)	517.14	660 Bearing Bronze	65	3.03	0.1-0.5
Bearing L1	1.5058 (3.825)	245.85	660 Bearing Bronze	65	3.03	0.1-0.5
Bearing B1	1.5026 (3.817)	517.14	Babbitt Coated 660	24	8.21	0.25-0.6
Bearing T1	1.5040 (3.820)	348.77	AISI 4140	197	1	0.25-0.7

From the data presented in Table 1, inserts S1 and S2 should have the least severe whip and whirl behavior because of their diameter and reduced friction coefficient. Even though analytical exercises show that the fundamental parameter in dry-friction instability is the friction coefficient, common knowledge is that a hard rotor rubbing on a soft stator is preferable to rubbing on a hard stator. Dry-friction testing on inserts comprised of different materials could indicate whether the severity of dry-friction instability is affected significantly by the hardness of the rub materials.

The axial length of the rub surface was selected to prevent multiple contact locations resulting from angular motion of the shaft. For the angular displacements predicted at the rub location, ½ in (1.27 cm) was sufficient to prevent rubbing on both sides of the rub surface.

BASE OF TEST STAND AND ROTOR SUPPORT

The components comprising the test apparatus were located on a massive test stand, which was softly supported to reduce orthotropy and provide a low natural frequency. These blue vibration isolators can be seen supporting the base of the test rig in Figure 9.

Figure 9 Test base supported on vibration isolators to reduce base natural frequency and orthotropy

The test rig was supported by a total of 6 vibration isolators, each having a stiffness of 788 $^{\text{lb}}/_{\text{in}}$ (138 $^{\text{kN}}/_{\text{m}}$). The base of the test stand weighed 2500 lb (1130 kg), which results in translational and rotational natural frequencies in the range of 3-6 Hz. Because the natural frequency of the base is significantly lower than the range of frequencies excited by dry friction, and the mass of the test stand is more than a hundred times that of the rotor, base motion is assumed to have little impact on the vibration characteristics of the rotor.

To account for the motion occurring in the test and support pedestals, impact tests were performed to measure their natural frequencies. These results are given in Table 2.

Table 2 First horizontal and vertical natural frequencies of the support and test pedestals

	Support Pedestal	Test Pedestal
Vertical Direction	1620 Hz	1240 Hz
Horizontal Direction	1000 Hz	615 Hz

The natural frequencies of the pedestals are in the range of frequencies that will be excited during whip and whirl; therefore, they could have a large impact on the whip and whirl motion and must be included in the model. Notice that the pedestals have a higher natural frequency in the vertical direction than in the horizontal direction. This indicates that the pedestals will provide an asymmetric stiffness to the rotor, which will also require caution during the modeling process. Previous studies by Lingener [12], Crandall [13] and Ghauri et al. [16] indicate that asymmetry may help to repress or eliminate dry-friction instabilities.

ROTOR DRIVETRAIN

During the initial phase of test rig design, simulations indicated the need for a powerful drive system capable of delivering high torques at low speeds. Additional program objectives mandated the capability to test transient characteristics of hydrostatic bearings during a rapid turbopump startup. This required a high speed motor capable of accelerating the rotor to 15,000 rpm in a matter of seconds. The selected motor had enough power to drive the rotor during dry-friction, but could not provide the torque expected from simulations throughout the desired speed range. The solution was a gear reducer. The primary components of the drive system are shown in Figure 10.

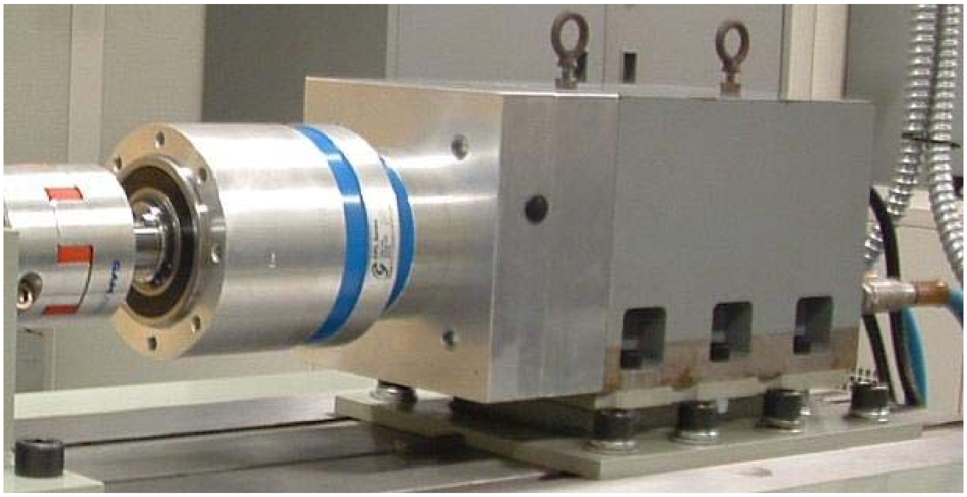

Figure 10 Drive system comprised of (left to right) coupling , gear reducer, and motor

The selected motor was manufactured by SKF precision technologies to drive high power machine tool operations. The motor can deliver 29.5 HP (22 kW) at a max speed of 20,000 rpm, and can apply a constant torque of 92.4 in-lb (10.5 N-m) throughout its operating range [37].

Simulations indicated that torques as large as 500 in-lb (56.5 N-m) were required to sustain dry-friction whip and whirl at rotor speeds from 0-240 rpm. A two-stage 25:1 EPL-NEMA-150 planetary gear reducer manufactured by GamGear was selected to accomplish this objective [38]. With an efficiency of 80%, the gear reducer could increase the drive torque to 1848 in-lb (210 N-m) for rotor speeds up to 240 rpm.

To connect the gear reducer to the test rotor, two GamGear EKM-Series elastomeric couplings were used in series with a spline shaft. The selected couplings are rated to transmit torques up to 4425 in-lb (500 N-m) and are designed to reduce backlash [39]. In addition, the couplings allow for the large range of radial and angular misalignments that could be created during whip and whirl. The spline shaft reduced the radial and angular stiffness of the support, which prevented the transfer of large rotor vibrations to the gear reducer and reduced the deflection due to misalignment between the gear reducer and the test rotor.

INSTRUMENTATION

As noted earlier, the instrumentation used to validate predictions of whip and whirl amplitudes consisted of four pairs of proximity probes located along the shaft, a pair of accelerometers mounted on each test pedestal, and a 64:1 encoder on the motor to detect rotor speed. All of the data was recorded using National Instruments Data Acquisition (DAQ) boards and post processed. More detailed information on these components can be found in Pavalek [40] and Dyck [15].

The proximity probes can be seen in Figure 8. The probes were oriented 45° from the horizontal and vertical directions, and were sampled at 20 kHz. This sample rate ensured that the predicted whip and whirl frequencies could be verified with adequate resolution. Probe pairs 1 and 2 located on the left and right sides of the test pedestal and probe pair 3 located on the magnetic bearing housing have a linear range of 70 mils, whereas probe pair 4 located in the support pedestal has a linear range of 8 mils. Due to its proximity to the support bearings, the amplitudes observed by probe set 4 should not exceed this limit.

The accelerometer pairs 1 and 2 are located at the top of the test and support pedestals, respectively. They are oriented along the same axes as that of the probes and are sampled at 20 kHz. The accelerometers can handle accelerations as large as 20g.

TEST SERIES AND DATA ANALYSIS

Several test series were executed for each stator insert consisting of linear speed profiles from 20 rpm $\rightarrow \omega_{max} \rightarrow$ 20 rpm, where ω_{max} was 140 rpm to 240 rpm. Some of the tests consisted of ascending or descending profiles; whereas, some consisted of both. The duration of tests was 30 to 90 seconds, which generated a sufficient number of data points in proximity to discrete rotor speeds for frequency analysis. The frequency analysis was accomplished by methodically searching for blocks of data having a desired mean rotor speed and taking a two-sided fast Fourier transform (FFT) of the block;

accuracy was determined by an acceptable standard deviation of rotor speeds contained in the block of data, which resulted in a range of ±1 rpm per block.

CHAPTER IV

SIMULATION MODEL

OVERVIEW OF XLTRC^2 ROTORDYNAMICS SOFTWARE PACKAGE

The simulations were performed using XLTRC2, a component-mode finite-element program that uses Timoshenko beam finite elements to generate a rotor and stator model [41]. The resulting dynamic system is composed of physical and modal coordinates, which enables the user to discard high frequency vibration modes while retaining physical coordinates at locations for nonlinear connections. For more information on component mode synthesis or XLTRC^2, consult Childs [42] or TAMU Turbomachinery Laboratory XLTRC^2 Brochure [43].

GENERAL SYSTEM MODEL

The XLTRC^2 simulation model for the TAMU Whip and Whirl Rig is shown in Figure 11. The model consisted of the test rotor, which is connected to the test pedestal at station 6 and the support pedestal at stations 25 and 27. Although a connection at the rub location is shown, this provided no linear stiffness or damping, and acted only as a location for the nonlinear connection. The test pedestals were modeled using a dummy shaft comprised of rigid massless elements, which provided the most effective mechanism to model the point mass stiffness and inertia properties of the two pedestals; This provided an asymmetric stiffness to the rotor.

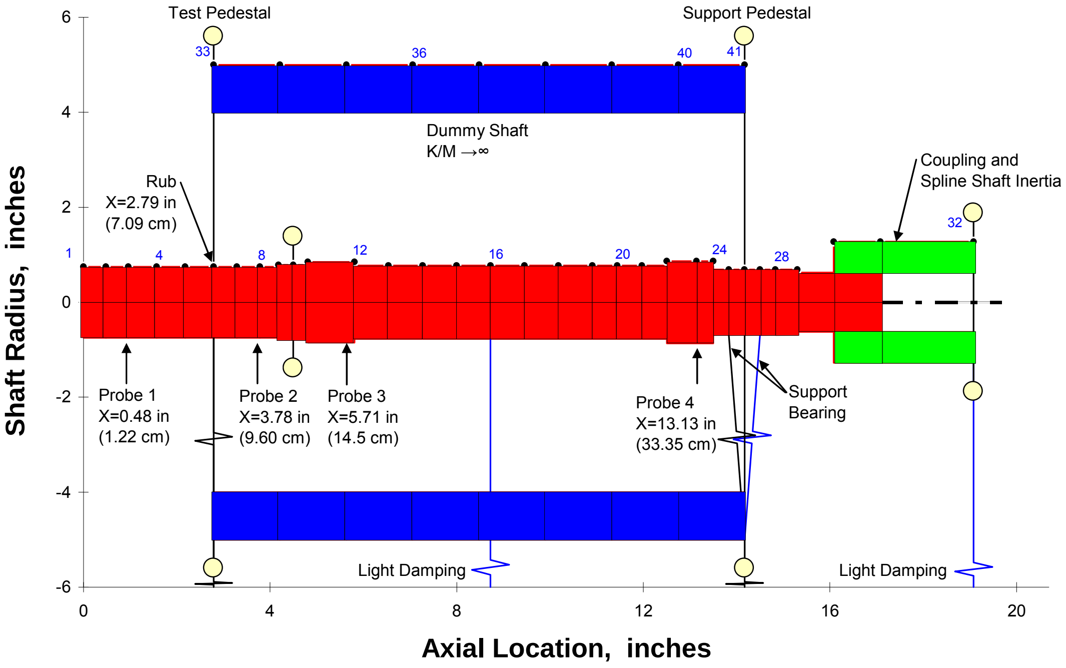

Figure 11 XLTRC^2 simulation model for TAMU Whip and Whirl Rig

SUPPORT ASYMMETRY

As noted in the description of the test rig, the pedestals introduce asymmetry into the system. To account for this in the model, an assumed mode for the lowest horizontal and vertical natural frequencies was used to estimate an appropriate point mass for each pedestal. Stiffness coefficients for each pedestal were determined using finite element analysis, and the resulting horizontal and vertical natural frequencies were compared with the experimentally determined values. Slight adjustments were then made to the model stiffness and mass coefficients to better reflect the frequency characteristics of the test rig. Even though asymmetry was accounted for in the model, note the limitations of the modeled system and its inability to reflect completely the structural properties of the rotor support.

VIBRATION CHARACTERISTICS

Although research investigating the effect of support asymmetry on dry-friction instability exists, a strong theoretical foundation has not been established. Black used complex receptances to predict regions in which dry-friction whirl could exist. This required that a solution be assumed for the whirl motion, which enabled the system to be reduced to a set of algebraic equations. Because self excited asymmetric motion often includes multiple frequencies, assuming a simple harmonic solution could prove misleading; however, assuming that the solution is dominated by some backward whirl frequency could provide some insight to the systems behavior. Proceeding with this assumption, a system with slight asymmetry would share the same dry-friction whirl regions as its symmetric counterpart; namely, dry-friction whirl can only exist in regions from one individual natural frequency to the next higher combined natural frequency. Table 3 presents the individual and combined natural frequencies and damping ratios for the simulation model. Neglecting the effect of damping, Table 3 suggests that the first possible whirl ranges are from 40.9 – 381.2 Hz, 429.6 – 565.7 Hz, and 606.5 – 786.0 Hz.

Table 3 Individual and combined vibration modes for the simulation model

Individual		Combined	
ω_n (Hz)	ζ	ω_n (Hz)	ζ
40.9	1.41%	381.2	1.03%
418.5	0.81%	392.3	0.93%
429.6	0.73%	565.7	2.23%
606.5	2.47%	786.0	1.07%
810.6	1.01%	868.0	0.48%
918.2	0.22%	1,142.3	2.45%
1,174.4	1.26%	1,164.1	1.40%
1,222.7	2.47%	1,612.7	2.01%
1,613.1	2.00%	2,264.5	1.42%
2,304.5	0.08%	2,296.1	1.56%
2,336.4	0.25%	2,675.9	17.03%
3,760.1	0.02%	2,710.4	16.42%

The full extent of these ranges will not be reached due to the presence of damping, but the system should lose the ability to maintain traction as it approaches any combined natural frequency. At these frequencies, the simulations should be marked by behavior that is independent of running speed until another whirl range is excited. Viscous damping was added to the model to ensure that the motions achieved by simulations were bounded and within the realm of those produced by the test rig. With the exception of the damping present for very high frequency modes, most of the vibration modes have close to a 1.0 % damping factor.

NONLINEAR CONNECTION

Nonlinear interaction at the rub location was modeled using a modified form of Hunt and Crossley's [25] coefficient-of-restitution model. Normal force was given by

$$N = k_{nl,1}\delta + k_{nl,2}\delta^2 + c_{nl}\dot{\delta}\delta \tag{17}$$

where $k_{nl,1}$, $k_{nl,2}$ and c_{nl} are nonlinear stiffness and damping coefficients and δ represents the deflection of the rub surface. This yields a transverse contact force

$$F_F = \mu N \operatorname{sgn}(V_t) \tag{18}$$

Where $\operatorname{sgn}(V_t)$ was first introduced by Bartha [19] to account for the relative transverse contact velocity. The nonlinear stiffness coefficients were determined from the derivative of the Hertzian contact force with respect to penetration depth. These terms depend heavily on the stator material and the diameters of the contacting bodies. The damping coefficient was obtained by scaling the experimentally determined parameters given by Bartha to yield comparable contact damping. The parameters employed in numerical simulations are given in Table 4.

Table 4 Nonlinear stiffness and damping coefficients employed in simulations

Nonlinear Stiffness $k_{nl,1}$ lb/in (N/m)	Nonlinear Stiffness $k_{nl,2}$ lb/in^2 (N/m^2)	Nonlinear Damping c_{nl} lb.s/in^2 (N.s/m^2)
5.71×10^6 (9.99×10^8)	1.03×10^{10} (7.10×10^{13})	2.40×10^5 (1.65×10^9)

One aspect of contact dynamics that has been neglected are forces arising due to rolling friction. Though these forces were found to be negligible in comparison to coulomb friction in literature, these sources looked at geometries closer to rail-wheel interaction in contrast to the bearing-race interaction present in dry friction. Rolling resistance could be significant for the latter case; however, as asserted by Bartha, a lack of available data ruled out the inclusion of these forces in the rub model.

SIMULATION PROCEDURE AND POST PROCESSING OF DATA

Whip and whirl behavior was simulated by exciting dry-friction whip and whirl at 235 rpm, running a simulation until a steady-state limit cycle persisted, then decreasing the rotor speed and running a new simulation from the previous state. This was performed recursively from 235 rpm to 20 rpm and back to 235 rpm. These constant speed data arrays were analyzed in the same manner as the experimental data and should be indicative of the measurements recorded by the probes and accelerometers on the test rig. The data recorded for each simulation consists of the position at each of the four probe locations and each pedestal. On the test rig, probe sets 1 and 2 were mounted on the test pedestal, and probe 4 was located on the support pedestal. To ensure that simulated probe data was as accurate as possible, the data recorded by probe sets 1 and 2 was relative to the test pedestal, and data recorded by probe 4 was relative to the support pedestal. This arrangement does not ensure that the motion seen by the probes during experiments are unaffected by the motion of the pedestals. Motion of the pedestals could consist of translational and rotational pitching and yawing motion, which would be difficult to simulate without a complete structural model of the support system.

SIMULATED BEARING CONFIGURATIONS

Table 5 shows three different simulations performed to facilitate comparisons for several test cases. These represent changes in bearing diameter and friction coefficient.

Table 5 Bearing parameters used in simulations

	Bearing Diameter in (cm)	Theoretical Whirl Frequency Ratio	Friction Coefficient	Comparable Test Cases
Simulation 1	1.5026 (3.817)	517	0.3	1-6
Simulation 2	1.5036 (3.819)	385	0.35	13
Simulation 3	1.5058 (3.825)	246	0.4	14-16, 20, 21

Friction coefficients were selected based on the ability to exhibit higher frequency whirl solutions, and should not greatly affect the nature of simulations upon subsequent increases. These elevated values will increase the range of whirl regions obtained and increase amplitudes at whip.

CHAPTER V

RESULTS

In this chapter, results for experimental whip and whirl motion will be presented, discussed, and compared to simulations. Test data will be presented first to illustrate the fundamental aspects of the whirl-whip motion as well as some characteristics previously unseen in literature. This will be followed by review of the simulation results and the models validity in simulating whip and whirl behavior.

EXPERIMENTAL DRY-FRICTION WHIP AND WHIRL CHARACTERISTICS

Due to the number of test cases, an abundance of test data exists. Presentation of test data has been constrained to cases having a certain degree of clarity, and has been organized by case number, probe number, and direction of speed traverse ("up" corresponding to accelerating and "dn" to decelerating). Appendix B contains a table of all test cases, and should be consulted for more information on each case.

Fundamental Observations on the Nature of Dry-friction Whip and Whirl

A representative dry-friction whip and whirl test case is shown in Figure 12 and Figure 13. Looking first at Figure 12, one notes that the system exhibits multiple whirl and whip regions. Both Lingener [12] and Choi [14] were able to excite a second whirl range; however, Choi was able to pass through an excited whip mode, whereas Lingener said this was not possible. This could have to do with the location Lingener was using to excite the second mode, the capabilities of the drive system, or some other unknown. The TAMU Dry-friction Whip and Whirl Rig readily passed through several whip regions; in some cases reaching frequencies as high as 2400 Hz.

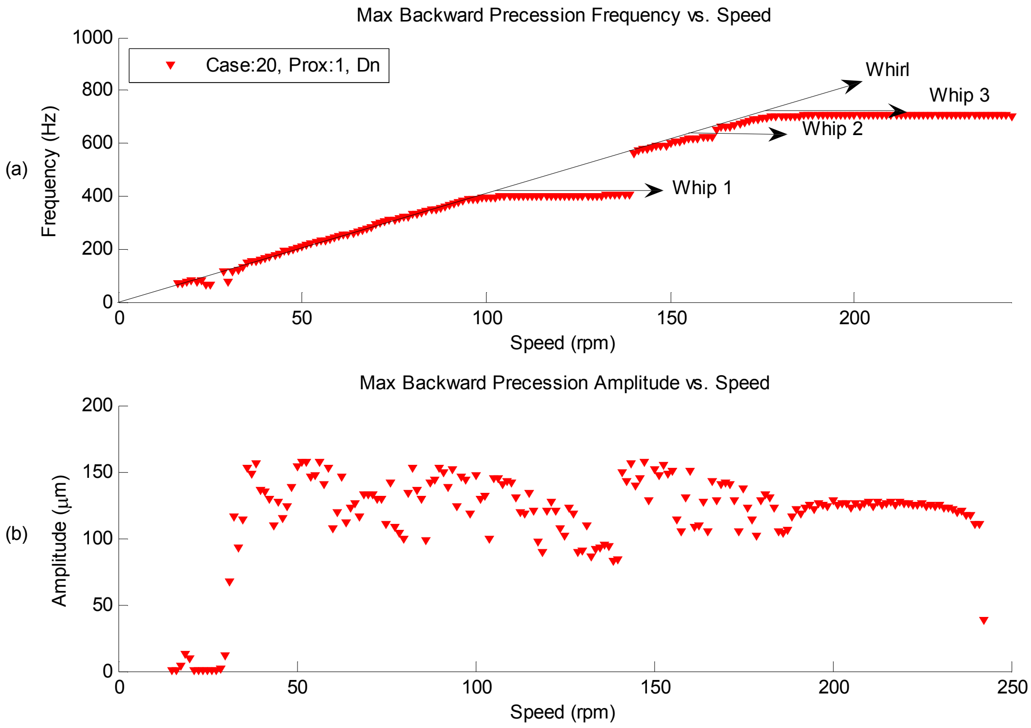

Figure 12 Measured (a) frequency and (b) amplitude of max backward whirl component at probe 1

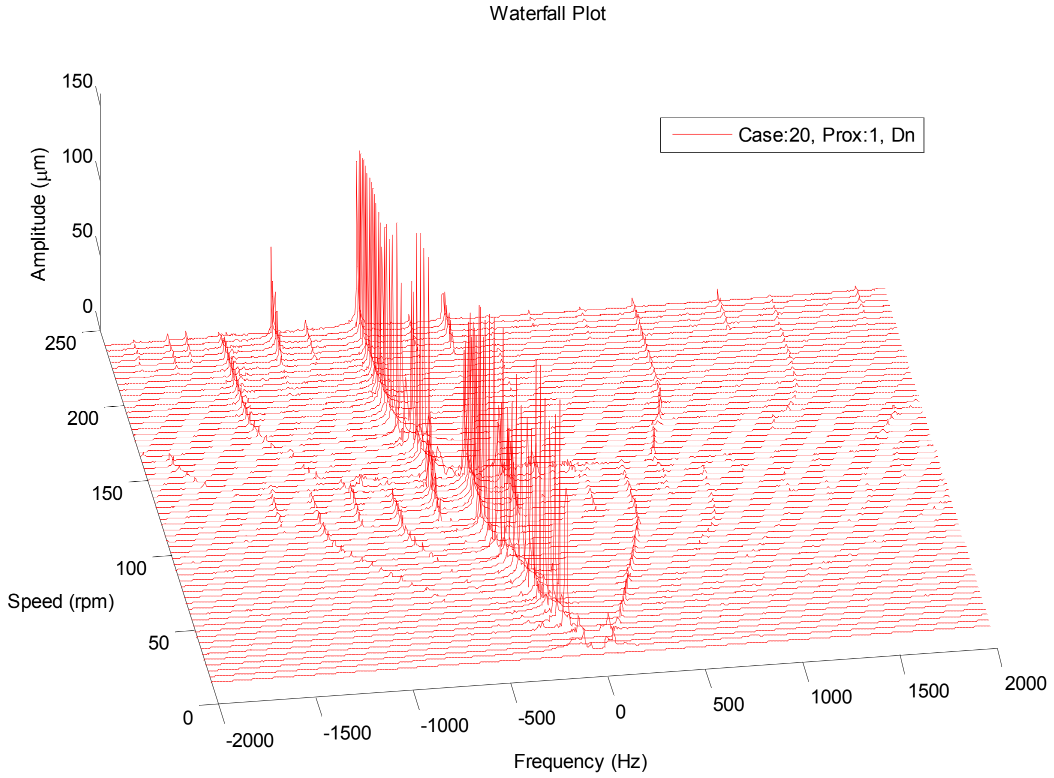

Figure 13 Two-sided FFT of probe measurements for typical case of dry-friction whip and whirl

Presence of Harmonic Sidebands Accompanying Primary Backward Component

Note in Figure 13 the sidebands that accompany the main backward whirl/whip component. The forward component at one times the main backward component (-1 Ω) can be attributed to the presence of asymmetry in the test rig. This creates an elliptical whirl profile, which can be described by forward and backward whirl components at the same supersynchronous frequency. This effect was more prevalent in smaller rub radii and other probe locations, which will be discussed in more detail later.

While the forward frequency component may arise due to asymmetry, this is not true of the backward components at multiples of the whirl frequency. These frequencies are a function of the main whirl component, and could be caused by the nonlinearity present in the stiffness deflection curve of the rub surface or by partial rubbing [44]. Consider the FFTs in Figure 13 at 120 rpm and 230 rpm, which are depicted in Figure 14. The system is in whip at these speeds, which indicates that the rotor is constantly slipping on the rub surface. If the relationship assumed for force versus deflection is investigated, an elliptical whirl profile could give rise to a 2Ω excitation, as well as sum and difference frequencies; these multiples can be seen in Figure 14a, which contains frequencies at ½ Ω, 1½ Ω, and 2 Ω at 120 rpm.

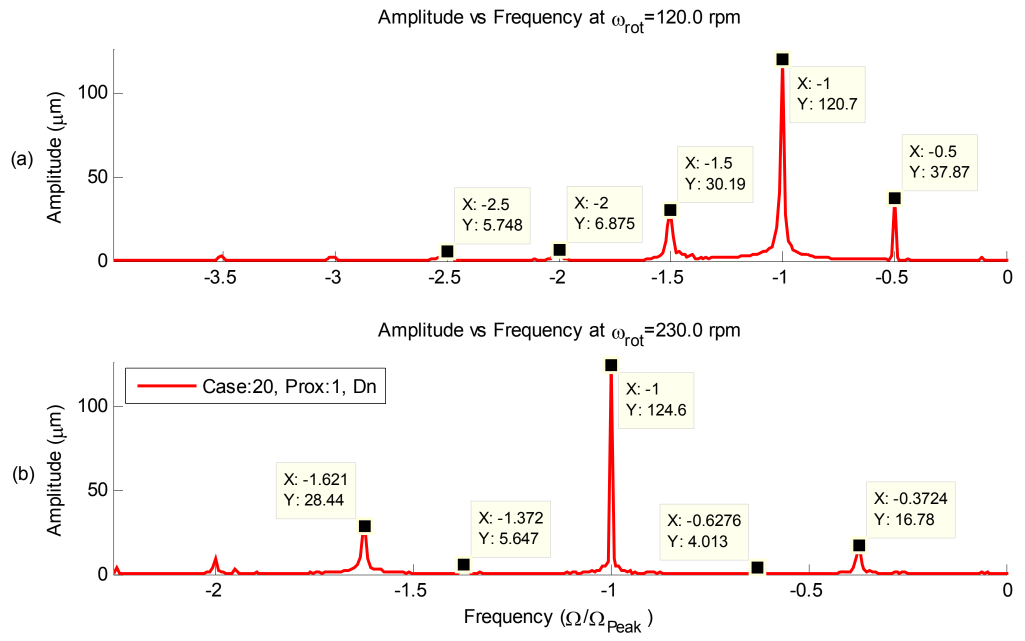

Figure 14 FFT of probe 1 measurements in whip at a) 120 rpm and b) 230 rpm rotational speeds

What is interesting about the spectrum presented in Figure 14b is that the rotor excites a different set of multiples in its third whipping region, shown here at 230 rpm. This spectrum includes multiples at 2Ω and 4Ω, but not the $\frac{1}{2}\Omega$ or $1\frac{1}{2}\Omega$ peaks present at 120 rpm; instead, it includes peaks at $\frac{1}{2} \pm \frac{1}{8}\Omega$ and $1\frac{1}{2} \pm \frac{1}{8}\Omega$, which is interesting. These could be caused by a difference in symmetry at the top and bottom of the test pedestal, in addition to the multiples presented by horizontal and vertical stiffness asymmetry. This effect might be more prevalent at higher frequencies because the $\frac{1}{2}\Omega$ harmonic is very close to one of the systems lower whip frequencies. Later, results will show that, when rotor speed is ascending in a whip region, these harmonic sidebands often excite the next whirl region.

Absolute and Relative Magnitudes Captured by Proximity Probes

What can be determined from the magnitudes captured by the proximity probes? From simply viewing the magnitude of the maximum backward component as a function of speed, as shown in Figure 15, one realizes the unsteady characteristics of the magnitudes captured by the probes.

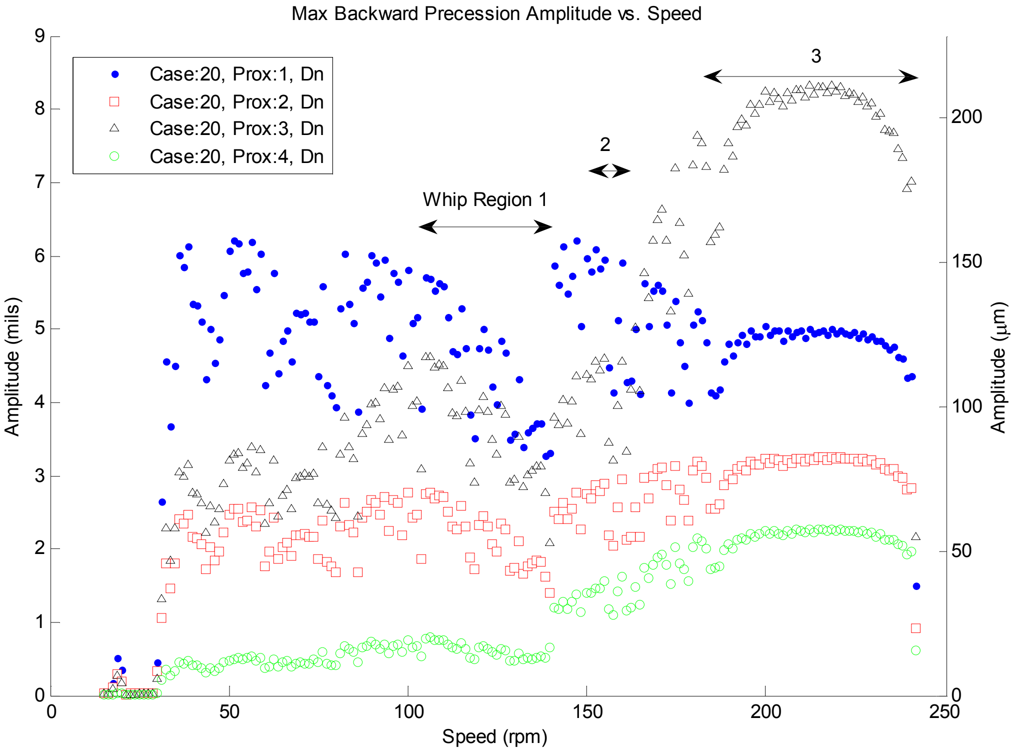

Figure 15 Measured backward precession amplitude versus speed

Does this represent unsteadiness in the whirl orbit obtained at a given rotor speed? Not necessarily; however, the magnitude of the orbit should not depend on the available friction coefficient at a given speed, so why are the amplitudes changing so drastically? Let us first examine whether the orbits in regions of whirl are attractive/stable. To do this, let us examine the magnitudes captured by the proximity probes relative to proximity probe 1, which is shown in Figure 16. This should give some indication of whether the magnitudes of the probes vary relative to one another, or simply on an absolute scale. If they do not vary relative to one another, then it must be assumed that the primary mode at a given speed is dominant.

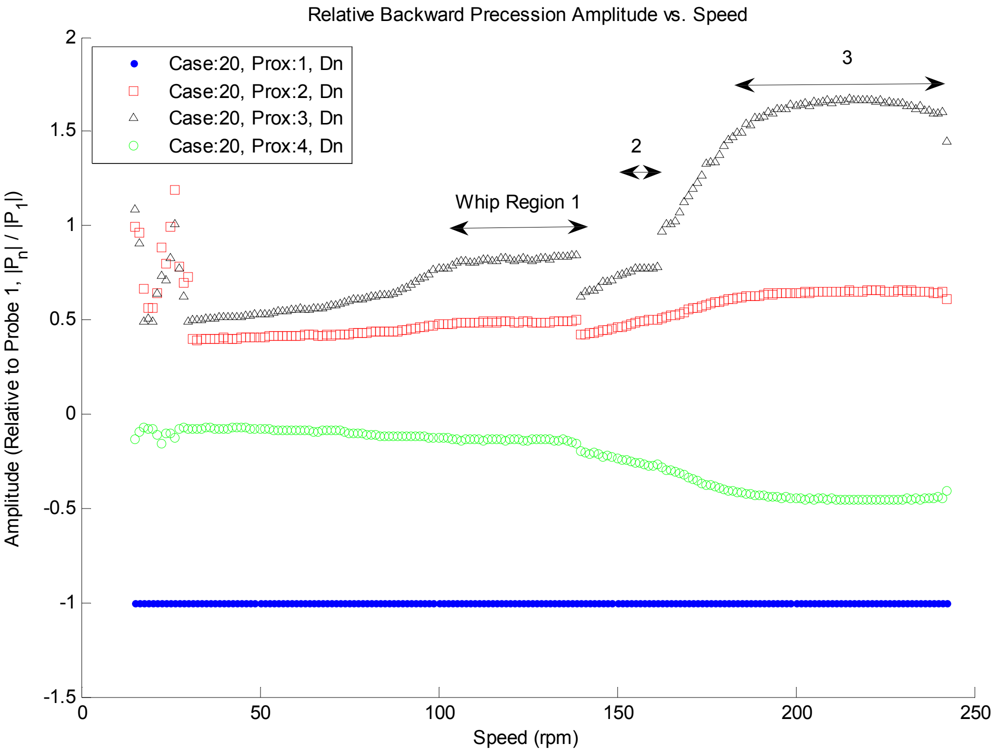

Figure 16 Measured backward precession amplitude relative to probe 1 versus speed

Figure 16 shows the following results: The discontinuities present in the relative magnitudes of the probes occurring at 140 rpm and 160 rpm are the speeds in Figure 12 that correspond to discontinuities in whirl frequency. These are the speeds at which the system switches whirl solutions, therefore ruling out its occurrence elsewhere in the speed range. Looking at the relative magnitudes also shows that, in regions of whip, there is no significant change among magnitudes. This consistency can be seen from 100-140 rpm, 150-160 rpm, and again from 190-240 rpm, and contrasts vividly with the change in absolute magnitudes recorded in regions of whip. Consider the change in absolute magnitude occurring during Whip Regions 1 and 3 shown in Figure 15. There is a steady decline in whirl amplitude throughout the entire range. This may correspond to the decline of friction coefficient that usually occurs with increased relative surface velocity or to the prominence of the whip solution over another solution. This issue will be addressed in subsequent discussion concerning the prevalence of one solution over another, but fails to explain the change of amplitudes seen in dry-friction whirl. How do the relative magnitudes recorded during whip compare to those predicted by the model's combined rotor-stator mode shapes? Figure 17 illustrates the measured and predicted modes in the first and third regions of whip shown in Figure 16.

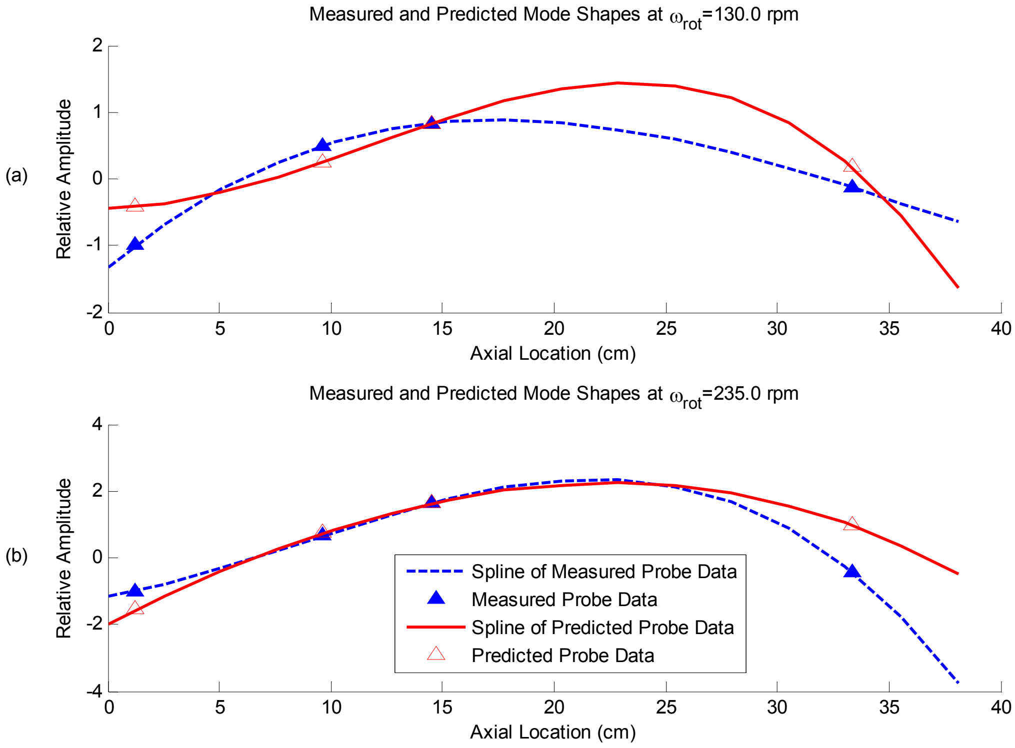

Figure 17 Measured and predicted relative mode shapes for Case 20 at a) 130 rpm and b) 235 rpm

The agreement between measured and predicted relative modes in the first whip region is weak; however, the third relative mode closely resembles test rig measurements. The model's inability to accurately predict the first mode might be attributed to the lack of pitch and yaw mobility in the test pedestal. Because the rub surface is located at the edge of the test pedestal, large contact forces could induce angular deflections and skew the measurements of Probes 1 and 2.

Figure 18 shows the physical orbits captured by the probes and accelerometers for Case 20 in the first and third whirl regions (a, c) and after transitioning to whip (b, d). At the time of this test, Probe 2 in the *X* direction and Accelerometer 1 in the *X* direction were not functioning properly. The accelerometer orbit was constructed by integrating with respect to the fundamental whirl frequency.

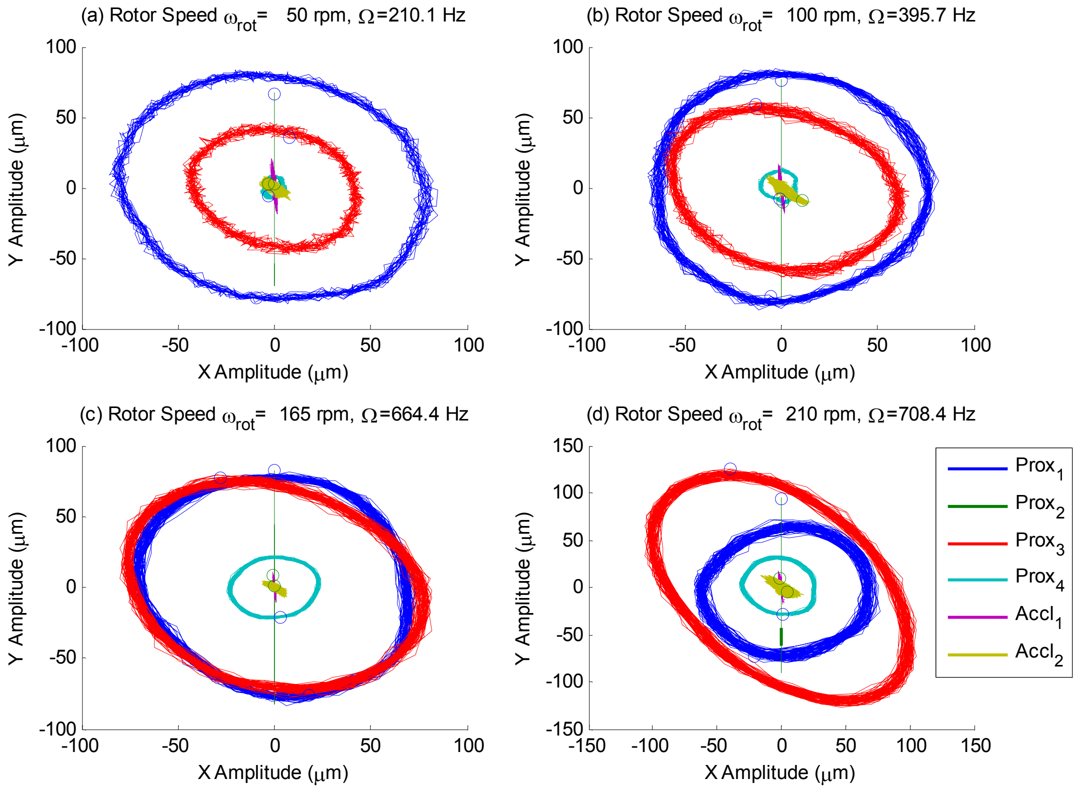

Figure 18 Measured probe and accelerometer orbits for Case 20 in a) the first whirl region, b) the first whip region, c) the third whirl region, and d) the third whip region

Figure 18 shows steady repeated orbits in both whirl and whip. In Figure 18d, Probe 3 and Accelerometer 2 show highly elliptical orbits with major axes in the horizontal direction (horizontal on the test rig at -45º). This may have prevented the rotor from transitioning to the higher frequency whirl solution that was excited in Case 21.

Predicted versus Measured Precession-Frequency Ratio (PFR)

The next topic to discuss will be the disparity between observed and predicted PFRs. Most sources state that the PFR (Γ) given in Eq. (1) should match the radius-to-clearance ratio at the rub surface. One might expect that the measured precession frequency would be slightly lower than this ratio due to a difference between the measured clearance and the actual radius of the rotors orbit due to contact deflection; however, no one has suggested that this ratio would be exceeded. Although not addressed in detail, Bartha [19] measured precession frequencies greater than that predicted by the PFR in at least one instance. The PFR for Case 20 presented above is shown as a function of speed in Figure 19.

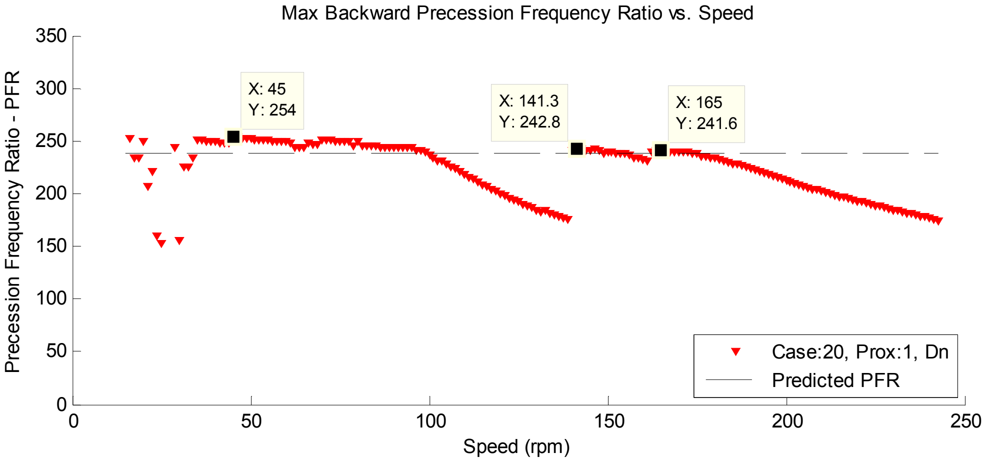

Figure 19 Measured precession frequency ratio versus rotor speed for large clearance bearing

The diameters of the rotor and rub surface were measured with calibrated instruments accurate to ± 0.1 mil (25.4 µm) prior to testing. For this case, the rub diameter was measured at 1.5060 in (3.825 cm), and the rotor 1.4997 in (3.809 cm). This predicts a PFR of 238. The measured PFR shown in Figure 19 reaches well above this value for each of the whirl regions. For the first whirl range, this constitutes greater than 6.7% of the whirl frequency. Even though the disparity seems minor, it becomes pronounced at higher whirl frequency ratios. Figure 20 presents a case in which the measured rub diameter was 1.5026 in (3.817 cm), resulting in a predicted PFR of 517.

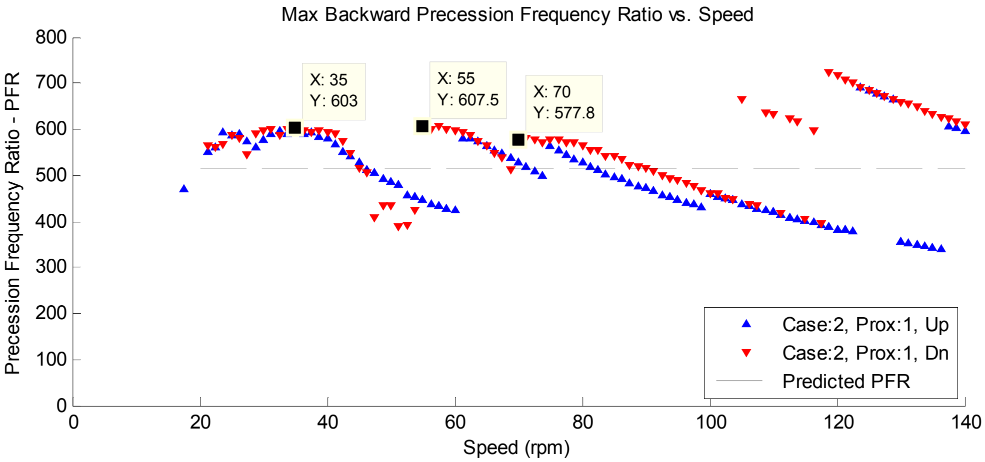

Figure 20 Measured precession frequency ratio versus rotor speed for small clearance bearing

Figure 20 shows the measured PFR is approximately 15-20 % higher than the expected value, which is significant. For dry-friction whirl in a realistic bearing, these deviations could be larger, possibly 30-40 % greater than the expected value.

The relationship between the predicted and observed precession frequency ratios becomes increasingly nonlinear with decreased clearances. Is the nonlinearity of this parameter an effect of increased sensitivity as clearance approaches zero, or is there some other explanation for this behavior? While the former is certainly true, Figure 21 illustrates a case in which the measured PFR rapidly increases to more than twice the predicted value.

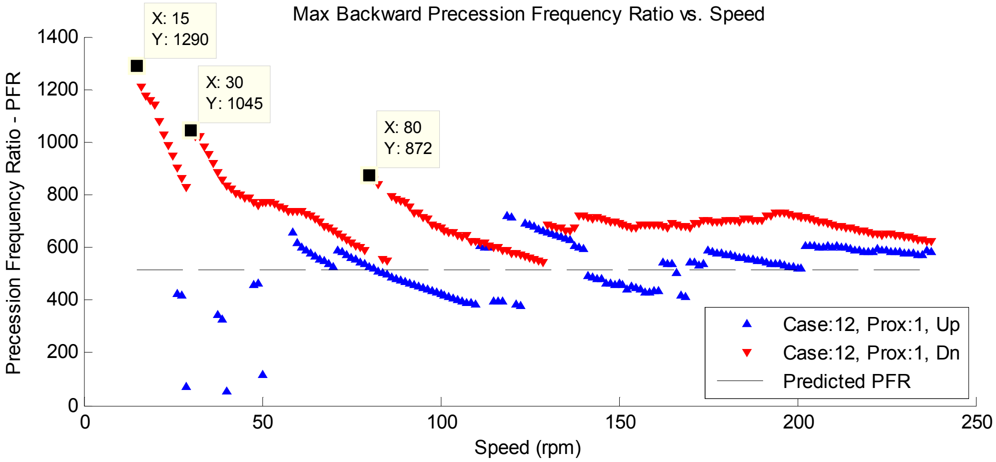

Figure 21 Measured precession frequency ratio for Babbitt bearing illustrating rapid increases at low speeds

Look closely at the measured PFR for the decreasing speed profile. As the rotor decelerates from 50 rpm, two instances occur in which the whirl frequency rapidly increases. This bearing had a predicted PFR of 517, which was exceeded by more than 150%! Although the reason for this unprecedented increase in observed whirl frequency ratio is unknown, deviations presented in other cases may have more rational explanations.

The measured whirl frequency ratio for Case 2 in Figure 20 is almost identical for increasing and decreasing speeds; however, this was not always the case. Case 3 in Figure 22 shows a significantly higher whirl frequency ratio for decreasing speeds than for increasing speeds.

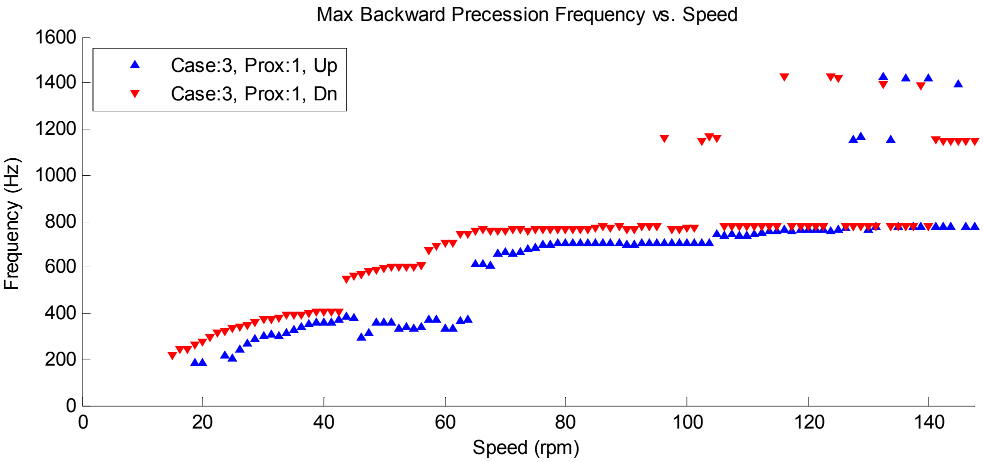

Figure 22 Increase in measured precession frequency ratio toward the end of test Case 3

This difference might be explained by thermal changes in the shaft or rub surface during the experiment. Due to the time delay between measurements, a slow increase in rotor temperature would result in decreased clearances toward the end of a test. Though thermal properties were not recorded, elevated temperature of the rotor or bearing was never perceptible by touch, excepting tests of a steel rub surface that resulted in seizure of the shaft. Case 3 supports the proposal that slow thermal variation may result in an increase in whirl frequency; however, other tests resulted in a significant amount of wear. This would tend to increase clearances and cause a decrease in observed whirl frequencies on the downward traverse. Figure 23 shows a decrease in observed whirl frequency toward the end of a case, which resulted in the removal of 3.5-4.0 mils (88.9-101.6 μm) of material from the bearing.

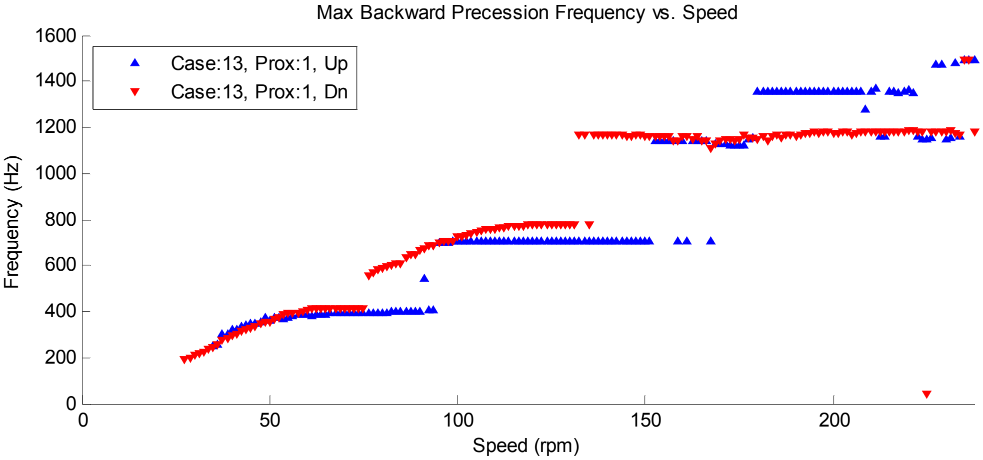

Figure 23 Decrease in measured precession frequency ratio toward the end of test Case 13

Existence and Excitation of Multiple Whirl Solutions

Billett [6] and Black [8] showed that sustained rotor-stator interaction due to dry friction was only possible for a limited range of frequencies. Outside of these ranges, the system was said to exhibit whip or loose contact. Black rationalized the stability of his whirl solution using the following argument. A shaft whirling on the U-shaped curve with increasing speed would increase in whirl frequency until the shaft could no longer maintain traction, causing the shaft to slip on the stator; conversely, a shaft whirling on the U-shaped curve with decreasing speed would persist until traction could no longer be maintained, resulting in the inability of the shaft to sustain whirl. Excepting studies of this depth on a rotor's ability to traverse a whirl region, few studies have been performed on the complexities encountered in the study of a realistic whip and whirl spectrum. These complexities include the presence of multiple modes and capability to excite them, the existence of multiple stable solutions, and complicated contact dynamics. These aspects will be discussed by observation of Case 21, which has a similar precession frequency ratio to Case 20 studied earlier.

Figure 24 illustrates the most apparent difference between increasing and decreasing speed profiles, namely the variability and extent of whirl regions with decreasing speed contrasted by the abrupt jumps encountered with increasing speed.

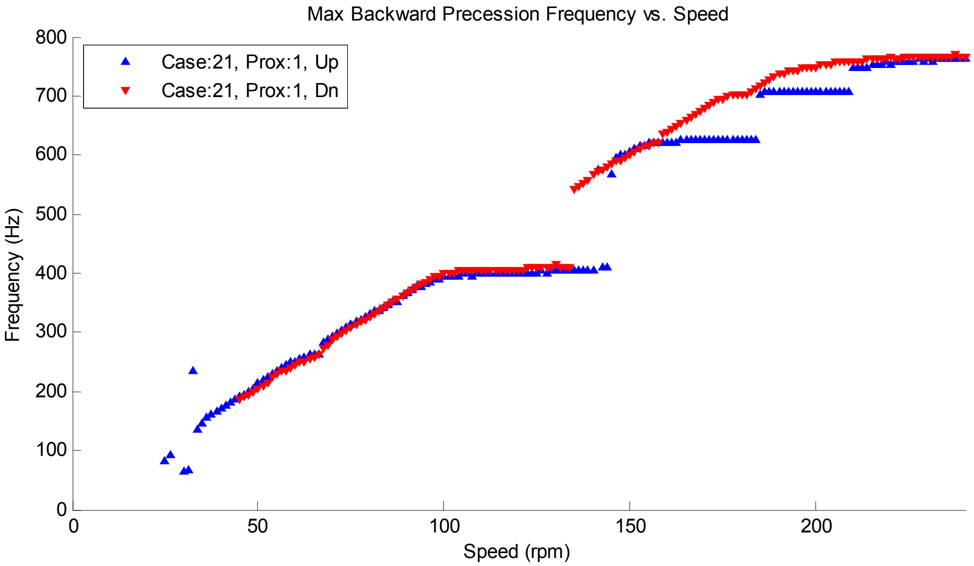

Figure 24 Measured backward precession frequency versus rotor speed at probe set 1

This result raises the following questions: (1) Why does the system appear to excite two whip regions when traversing down but four on the way up? (2) Why, if the first/lowest whip orbit is stable/attractive, does increasing rotor speed result in a jump to a higher whirl frequency, and what causes this jump?

In response to the first question, one must review the vibration properties of the test rig. The lowest measured natural frequencies of the test and support pedestals were 615 Hz and 1000 Hz. These were measured without the rotor in place; therefore, the addition of the rotors mass to the system would reduce these values. These are likely the whip regions that are not excited by the downward traversing rotor, assuming that neither of these modes involves unaccounted angular deflections of the pedestals. These regions were not excited by the descending rotor for the following reasons: The difference between individual and combined natural frequencies for a system composed of a massive-stiff pedestal and a relatively light rotor will be minimal, thus the range of unattainable whirl frequencies between the combined and next higher individual natural frequency will also be minimal. In addition, these modes have relatively little damping, thus the reduction in range caused by deficient traction is small.

The first step toward answering the second question is to examine the nature of the harmonic sidebands present in the frequency spectrogram in Figure 25.

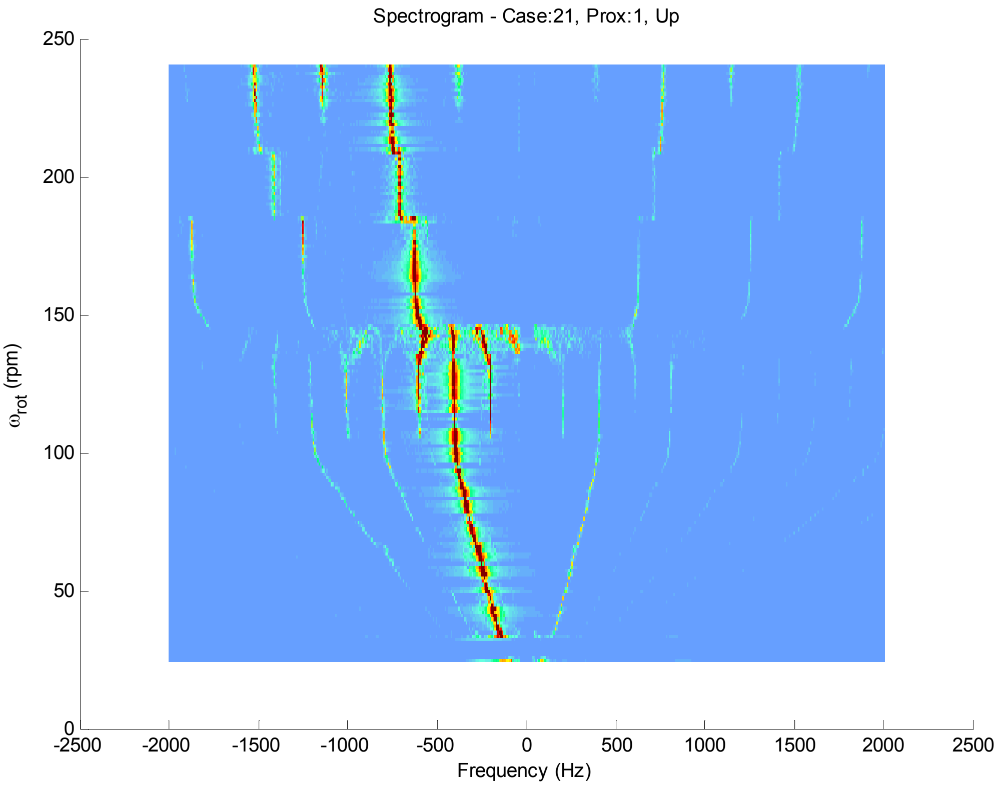

Figure 25 Spectrogram plot showing excitation of higher whirl modes by sideband harmonics

Although sidebands are present throughout the rotor's first whirl region, an additional set of sidebands is excited upon entering the first whip region. As the rotor approaches 137.5 rpm, the $1\frac{1}{2}$ Ω harmonic sideband begins to migrate toward the whirl solution, provided in Figure 26 by the speed-decreasing whirl component. At 142.5 rpm, the sideband reaches this whirl frequency and begins to excite it. At 147.5 rpm, whirl is fully excited, causing it to become predominant.

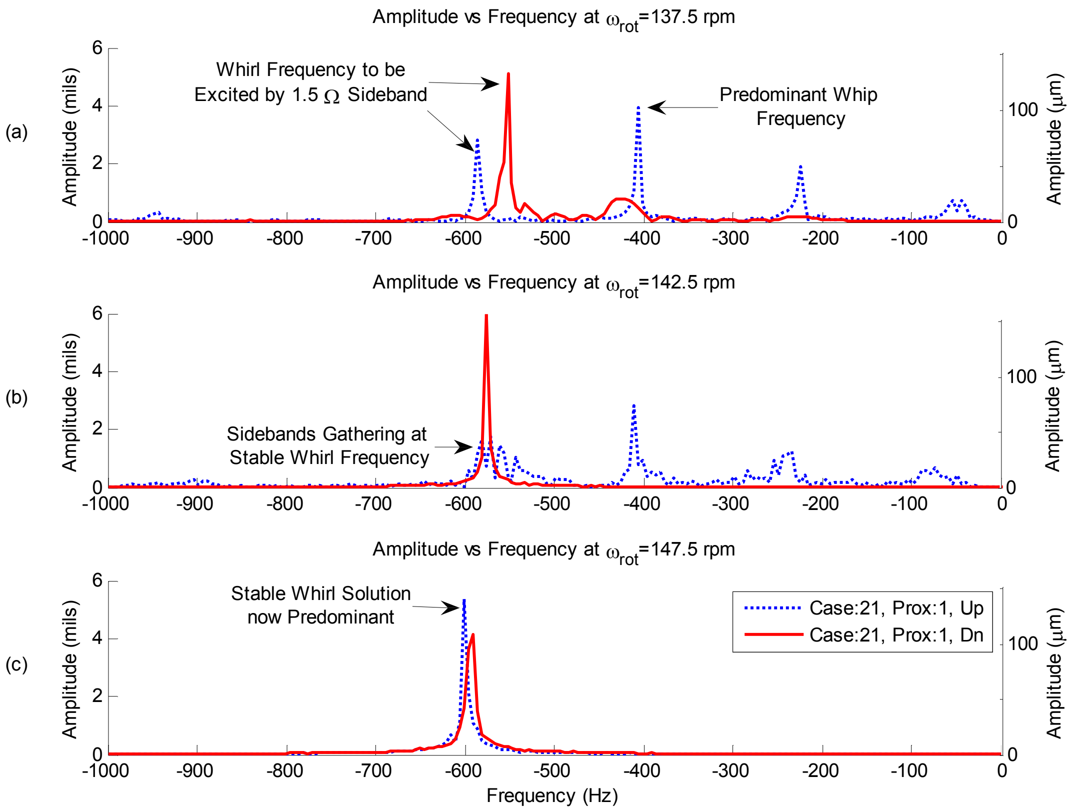

Figure 26 FFT at (a) 137.5, (b) 142.5, and (c) 147.5, showing harmonic sideband excitation of a higher whirl mode

The physical orbits captured during this speed range are shown in Figure 27. The whip solution shown in Figure 27a is steady and repetitive; however, increasing speed induces a 2Ω harmonic that eventually excites the 605.8 Hz whirl motion illustrated in Figure 27d. The competing whirl orbits in Figure 27 (b,c) might be the cause for the decrease in amplitude during whip discussed earlier.

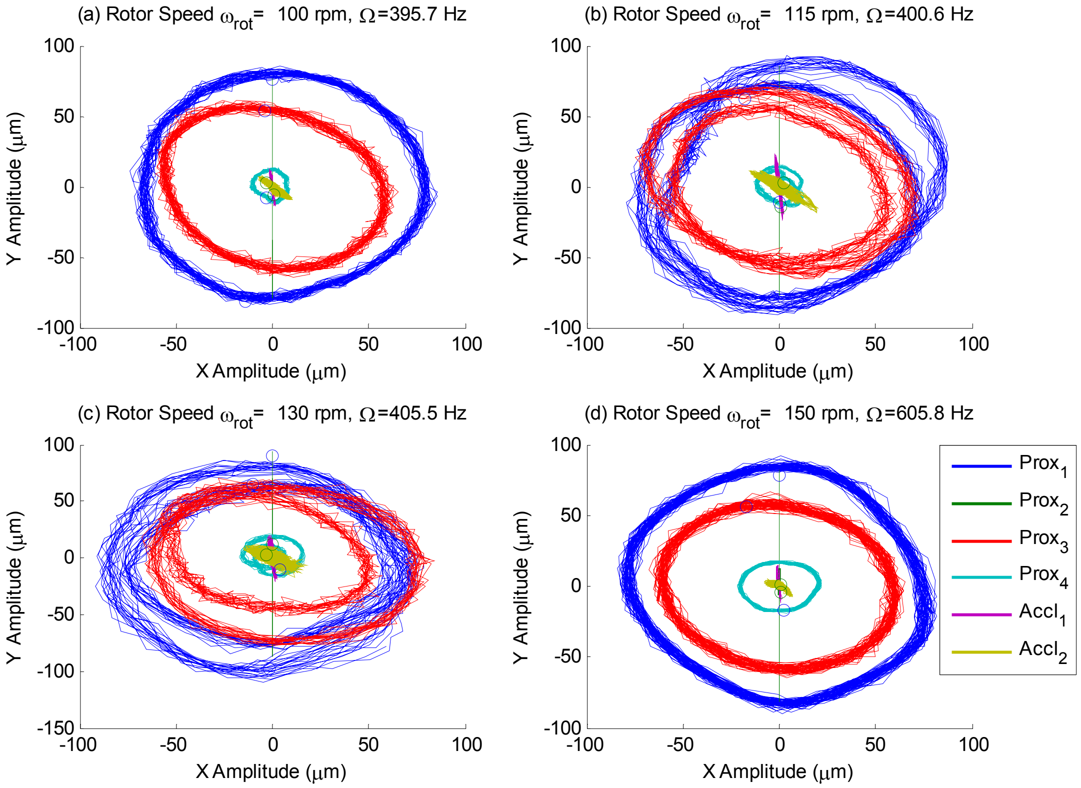

Figure 27 Physical orbits captured by probes during whip showing unsteady characteristics

Why is preference shown to one solution over another? The most likely explanation is the relationship between relative surface velocity and coulomb friction. An increase in relative surface velocity between two bodies usually corresponds to a decrease in available traction angle [19], thus favoring solutions based on their proximity to whirl. The spectrogram in Figure 25 shows that sidebands are not a necessary element to induce a frequency jump. In jumping from the second to the third whip frequency, a jump is excited simply by proximity to whirl.

A jump to orbital frequencies nearest in proximity to whirl was not always seen, as shown in Figure 28. This case represents a response of the Babbitt-coated surface that was excited at 250 rpm, previously seen to excite a surplus of whirl regions throughout its traverse.

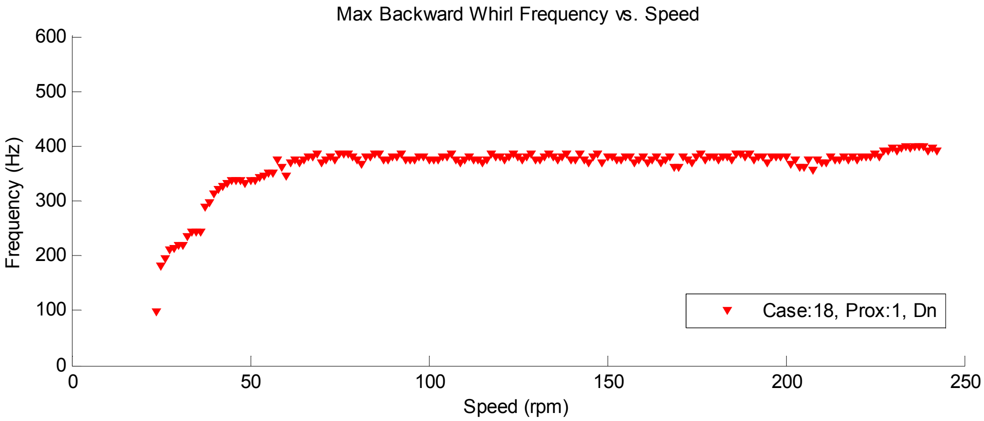

Figure 28 First whip mode for Babbitt bearing prevalent over higher modes

SIMULATION VALIDATION

How does the simulated whip and whirl behavior compare to the measured whip and whirl data? Before comparing results to predictions, a few inconsistencies must be addressed. The most significant discrepancy between simulated and experimental whip and whirl data is the nature of data analysis. While a group of experimental data was taken in close proximity to a rotor speed, the frequency spectrum represents a range of speeds. This contrasts with simulation data, which corresponds to motion at a specific rotor speed. This difference will tend to increase the bandwidth of an observed peak and decrease its magnitude in experimental analysis. The second proviso that must be placed on data comparison concerns the variation of friction coefficient in experiments versus a constant friction coefficient in simulations. This difference could skew the amplitude and frequency of whip and whirl orbits in experimental data because both depend on the available friction coefficient. Last, remember that the extreme amplitudes experienced in experiments could have placed some sensors outside of their linear range. Two of the probes were destroyed due to contact with the rotor, which occurred during late test cases. Vibrations caused these probes to loosen and shift towards the rotor, resulting in contact at a decreased clearance.

Whip and Whirl Frequencies

The first comparison between experimental and simulation data will be the main component of precession frequency versus rotor speed. Figure 29 shows a comparison between Simulation 2 and Case 13, which have the same predicted precession frequency ratio.

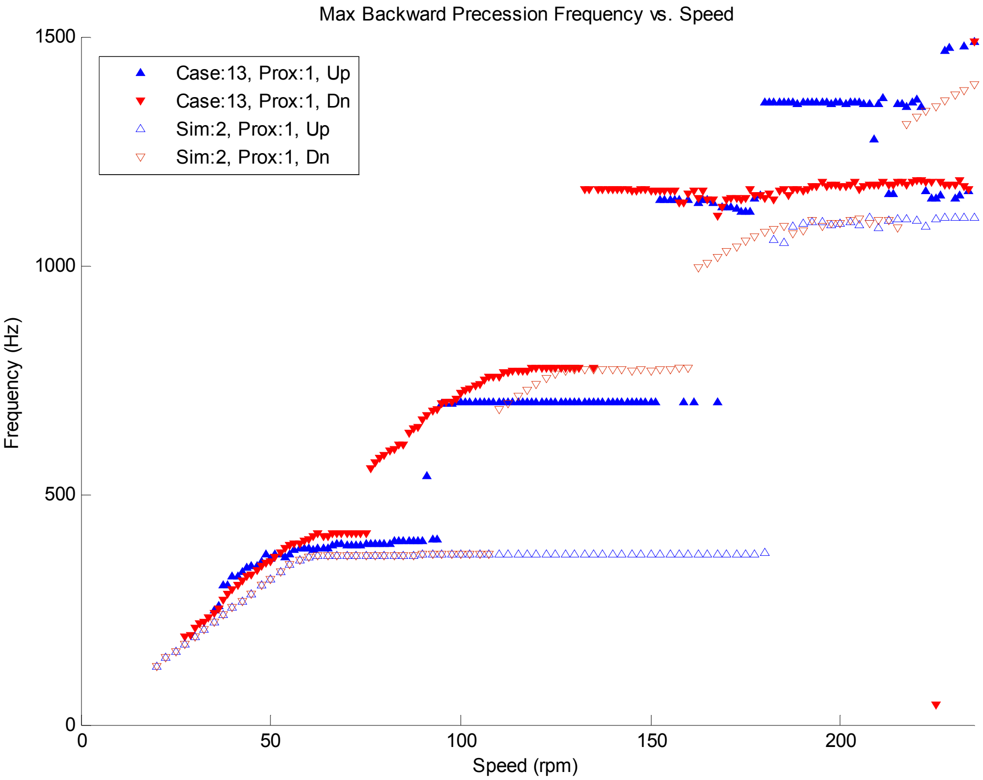

Figure 29 Comparison of measured and predicted backward precession frequencies

From this plot, the difference between the actual and predicted precession frequency is evident, appearing slightly higher for the test case. Even though this difference affects whirl frequencies, the frequencies at which the simulation and experiment transition to whip are very close, deviating only at frequencies above 800 Hz; this deviation could occur due to unknown structural properties. The simulation model does not excite the second whirl/whip region, despite the observation of this mode in test data. This whirl region is located from 429.6 – 565.7 Hz, and lies between the first and second bending modes of the rotor. This mode is characterized by large deflections at the pedestals, which were damped in the model to ensure that motion was within reasonable limits. The increased damping of this vibration mode could explain the absence of this whirl region in simulations. Overall, the whirl orbits obtained in simulations approximate within reason the orbits measured in experiments.

Amplitude Comparison

Figure 30 shows the amplitudes obtained during a simulation of the bearing used in Cases 20, 21.

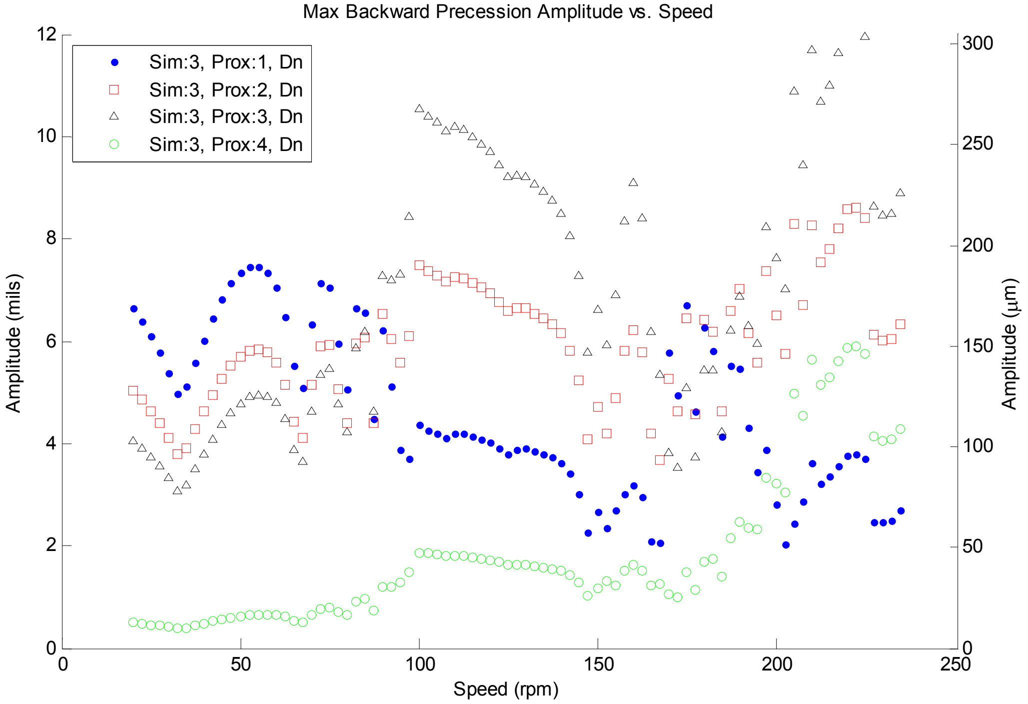

Figure 30 Predicted backward precession amplitude versus speed for all probes

In comparison to actual amplitudes given in Figure 15 for Case 20, the simulations produced slightly larger amplitudes. In addition, the simulations produced a more fluid absolute amplitude plot; whereas, experimental measurements were quicksilver in nature. Figure 31 illustrates simulation data comparable to the test data given in Figure 16.

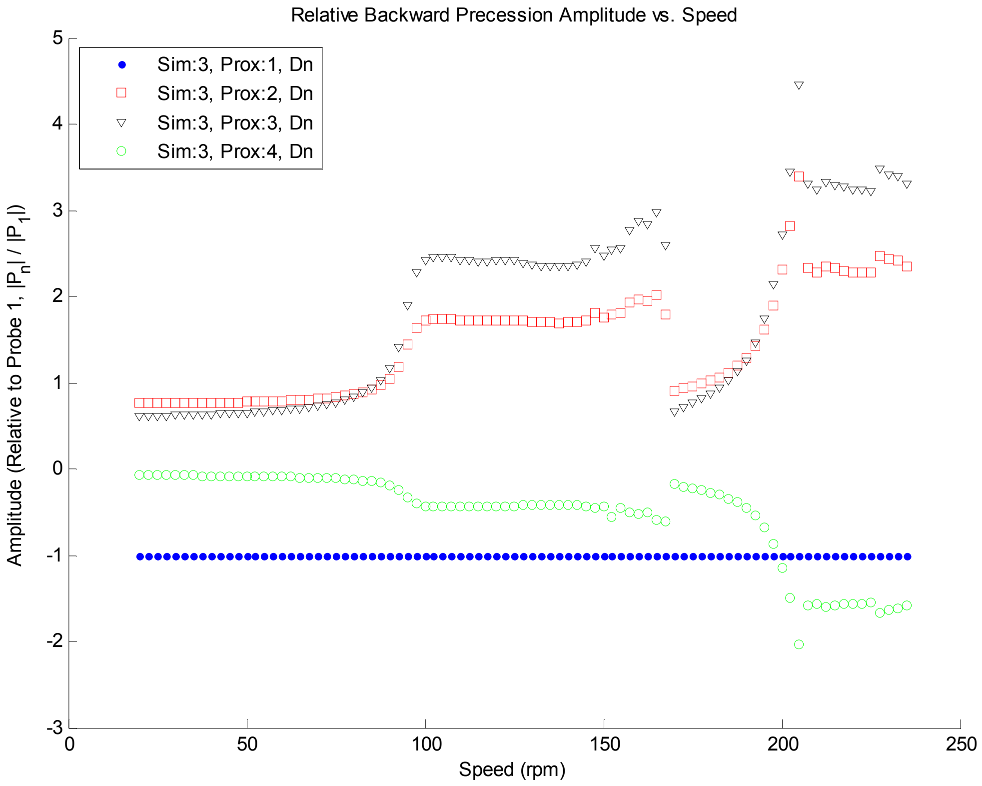

Figure 31 Predicted backward precession amplitude relative to probe 1 versus speed for all probes

By comparison to the experimental data, the amplitudes measured at probe 1 are significantly larger than in simulations. This variation could be a result of a difference between the actual and theoretical rub locations. The theoretical rub location was the center of the rub surface; however, during different modes, the actual rub location could have been located on the outside or inside of the rub surface. This could affect both the observed amplitude, and excitability of a given solution. Another aspect that could affect comparison of probe measurements includes pitch and yaw rotation of the test pedestal, which was not accounted for in simulations. A side by side comparison of the measured and predicted relative amplitudes is shown in Figure 32.

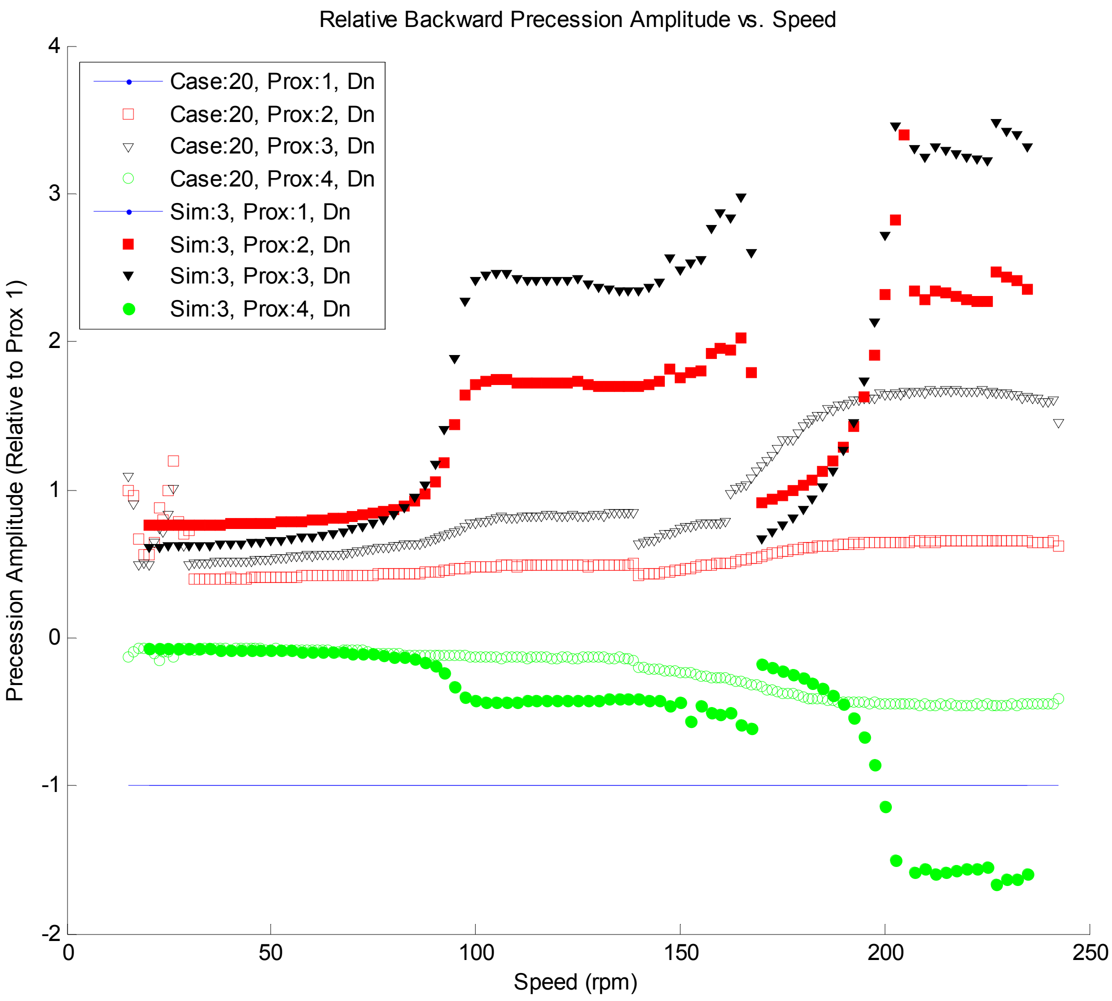

Figure 32 Predicted and measured backward precession amplitude relative to probe 1 versus speed

Nature of Frequency Spectrum

Figure 33 shows a waterfall plot for vibrations predicted in Simulation 2. The comparison of simulation frequency spectra as compared to experiments reveals that there are harmonic sidebands predicted during whip but not during whirl. In addition, the sidebands seem to be drastically different during higher-frequency whip regions than observed in experiments. Overall, the spectra bear good resemblance to their experimental counterpart.

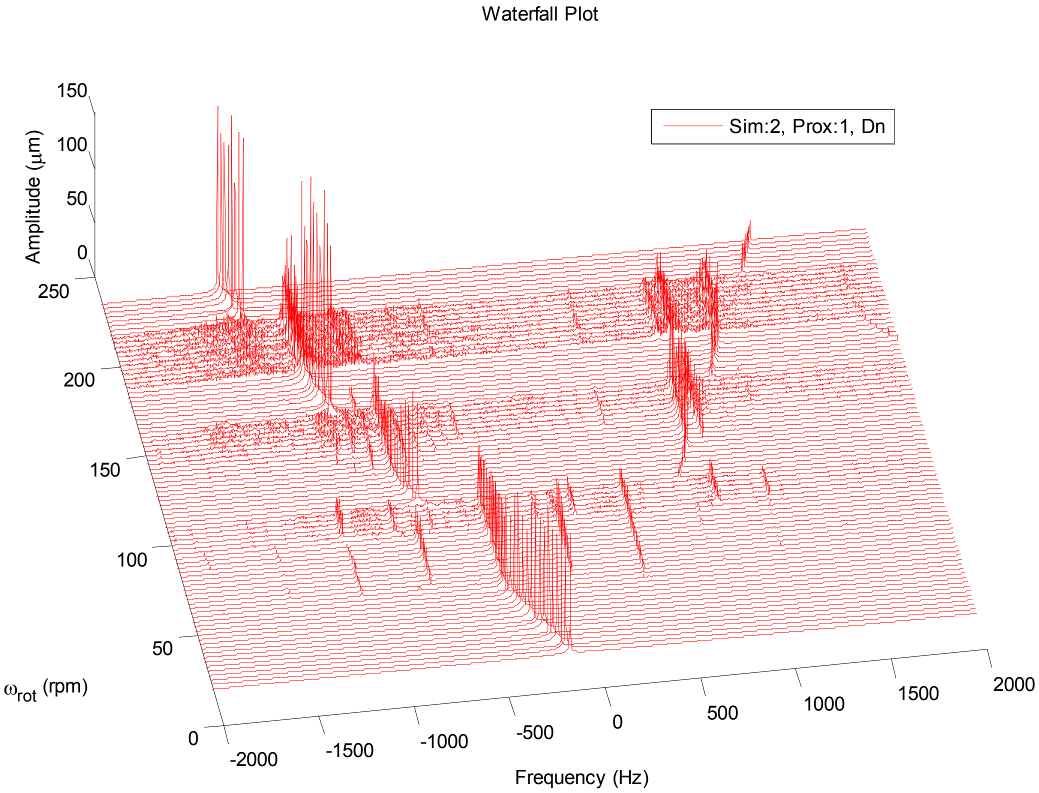

Figure 33 Frequency spectra for simulation 2 at probe 1

CHAPTER VI

CONCLUSION

The present thesis looks at characteristics unique to the phenomena of dry-friction whip and whirl and the ability of modern simulation tools to accurately model the instability. This chapter will present the accomplishments provided by the research and recommend focal points for future investigations.

EXPERIMENTAL ACHIEVEMENTS

Through the cumulative effort of the author, Dyck [15], Pavalek [40], and affiliated researchers, a dry-friction whip and whirl test rig was designed and constructed that demonstrated and recorded accurately the nature of multi-mode dry-friction whip and whirl. The test-rig's drive system could deliver accurate acceleration and deceleration profiles while sustaining dry-friction instabilities. This was accomplished by employing accurate feedback control to a 30 HP motor and attached gear reducer to deliver torques up to 1848 in-lb (210 N-m) for rotor speeds up to 240 rpm. Design of the test rig enabled the testing of several rub surfaces to examine the effect of bearing material and clearance on dry-friction whip and whirl. The data obtained on the TAMU Whip and Whirl Test Rig is the best available for dry-friction whip and whirl behavior.

ON THE NATURE OF MULTI-MODE DRY-FRICTION WHIP AND WHIRL

Analysis of experimental data provided by the test rig revealed several interesting facets of dry-friction whip and whirl in a realistic machine. Some of these conclusions echo fundamentals established by previous authors; however, others have no precedent and are founded solely on data provided by this work.

The results confirmed that dry-friction motion falls into the following regions:

- Dry-friction whirl in which the precession-frequency ratio is roughly proportional to the radius-to-clearance ratio at the contact location.

- Dry-friction whip in which the rotor precesses at a frequency close to a combined natural frequency of the connected rotor and stator system.

These regions, however, were not solely defined by rotor speed due the existence of multiple attractive orbits at a given rotor speed. The rotor speed can increase and decrease through regions characterized by whip, terminating with jumps to different whirl/whip frequencies. These frequencies are usually close in proximity to the predicted whirl frequency, which are assumed to have a higher friction coefficient due to a reduction in rotor-stator relative surface velocity [19]. The possibility of a jump alone was not sufficient to guarantee one, as some cases maintained a constant whip frequency throughout several possible whirl ranges. The failure to excite higher modes in these cases was possibly a lack of friction, created by some unknown environmental variable.

In observation of the frequency spectrum provided by probe data, the presence of harmonic sidebands was noted. They are suspected to result from structural asymmetry of the test pedestals in combination with the nonlinear stiffness provided by the rub location. These harmonics became more prevalent in whip, sometimes exciting higher whirl frequencies.

Data analysis shows measured precession-frequency ratios that are greater than those predicted by the radius-to-clearance ratio at the rub surface. This deviation was minimal for larger clearances while becoming pronounced for smaller clearances. Some variation in these values might be attributed to changes in thermal properties of the system or wear of the rub surface, while others are unexplained. Rapid increases of the measured whirl frequency ratio were noted for some cases having large radius-to-clearance ratios, reaching 250% the predicted precession frequency ratio.

Dry-friction whip and whirl testing on different bearing configurations resulted in a variety of whirl frequency ratios and whirl ranges; however, the frequencies at which the shaft whipped were constant for all test cases.

ON THE VALIDITY OF THE SIMULATION MODEL

The ability of the simulation model to produce accurate whip and whirl characteristics relies on two aspects. First, the model must properly account for the structural properties of the system to be examined. Second, the model used to represent rub must accurately describe the characteristics of the actual rub surface.

As to the suitability of the model in accomplishing the first objective, the model performed adequately. The simulations accurately predicted the first few fundamental modes of the test rig, resulting in very accurate whip and whirl regions through the second rotor mode at 800 Hz. Although there were deviations between predicted and observed motions, improvements would require the development of a more sophisticated structural model of the test stand; this improvement would require the utilization of commercial structural analysis tools. The most significant failure of the structural model was the inability to excite one of the intermediate modes that was seen in experiments. This failure could be a result of improper modal damping, which was intentionally increased to yield acceptable motions of the pedestals, or the friction coefficient used in the rub model. The amplitudes produced by the test rig were slightly smaller than those seen in simulations. This was attributed to the nature of data processing, as well the lack of detailed structural properties of the test stand.

In light of the characteristics that have the greatest significance, the nonlinear contact model and applied coulomb friction perform adequately. The deviation between actual and theoretical whirl frequencies illustrated by test data is not a characteristic that is exhibited in simulations; the simulations abide closely to the predicted whirl frequency ratio, deviating only slightly when approaching whip.

Overall, the ability of the simulations to yield accurate whip and whirl frequencies and amplitudes relies on the ability to model accurately the structural properties of the system and the rub surface. For the model used to simulate whip and whirl behavior for the TAMU Dry-friction Whip and Whirl Test Rig, comparisons were deemed acceptable.

DIRECTION FOR FUTURE RESEARCH

There are several topics that could be addressed to further improve the fundamental knowledge and predictive capabilities of dry-friction whip and whirl. These topics include a mixture of theoretical, experimental, and numerical investigations on the subject.

Development of a More Accurate Rub Model

A parametric investigation of the whirl frequency ratio as related to bearing clearance, clearance ratio, material, and whirl frequency would help in the development of a more accurate mechanical rub model. Such a model might accurately predict the complex dynamic reactions present at the rub surface, and would likely require the use of a finite element rotor and stator at the rub location. Additional improvements to the rub model include modeling thermal changes and surface wear. In some cases, a significant amount of material was removed from the surfaces of the bearing; this resulted in dry-lubrication of the contact surfaces and ultimately diminished or prevented subsequent dry-friction whirl.

Experimental investigation of dry-friction motion with the capability to measure the thermal properties of the rotor and rub surface would help to establish the importance of temperature during dry-friction whip and whirl. These properties are important not only due to their affect on dimensional quantities, but on the friction coefficient, elastic modulus, and fracture mechanics of the rubbing surfaces.

Inclusion of a Sophisticated Structural Model

One of the largest unknown factors encountered in the modeling process was how to accurately model the structural properties of the base of the test rig. Isolating the base of the test stand using soft supports prevented the transmission of large forces to the ground, thus allowing the base of the test stand to be modeled as an inertial frame. The difficulty was in accounting for motion occurring between the contact locations in the test and support pedestals. The solution was to model each pedestal as a single mass system, having horizontal and vertical natural frequencies similar to those observed on the test rig. This resulted in the dismissal of torsional modes, which were certainly activated due to the location of the rub surface in the test pedestal and the cantilevered bearing in the support pedestal. The ability to accurately include the structural properties of the support in the simulation model would greatly improve the accuracy of the predicted motions.

NOMENCLATURE

AFRL	Air Force Research Laboratory	
ALH	Advanced Liquid Hydrogen	
AMB	Active Magnetic Bearing	
C_r	Radial Clearance at the Rub Surface	in (m)
F_F	Friction Force at Contact Location	lb (N)
FFT	Fast-Fourier Transform	
N	Normal Force at the Contact Location	lb (N)
NGST	Northrop Grumman Space Technology	
O_r, O_s	Center of the Rotor and Stator	
$\boldsymbol{P}$	Complex Contact Force	lb (N)
P&W	Pratt & Whitney	
PFR	Precession-Frequency Ratio	
R	Rotor Radius at the Contact Location	in (m)
RSR	Rotordynamics Seal Research	
V_t	Relative Tangential Surface Velocity at Contact	in/s (m/s)
TAMU	Texas A&M University	
USET	Upper Stage Engine Technology	
$\boldsymbol{Z_r}$, $\boldsymbol{Z_s}$	Complex Rotor and Stator Displacements	in (m)
a	Rotor Mass Imbalance	in (m)
c_{nl}	Nonlinear Contact Damping	lb.s/in^2 (N.s/m^2)
c_r, c_s	Rotor and Stator Damping Coefficients	lb.s/in (N.s/m)
e	Shorthand for Exponential Function $e^{\ln(x)}=x$	-
$\boldsymbol{j}$	Imaginary Unit $j=\sqrt{-1}$	-
$k_{nl,1}$, $k_{nl,2}$	Nonlinear Contact Stiffness	lb/in, lb/in^2 (N/m, N/m^2)
k_r, k_s	Rotor and Stator Stiffness	lb/in (N/m)
m_r, m_s	Rotor and Stator Mass	lb.s/in (kg)
t	Time	s

x_r, x_s	Rotor and Stator Displacements Along the x-axis	in (m)
y_r, y_s	Rotor and Stator Displacements Along the y-axis	in (m)
$\boldsymbol{z_r}$, $\boldsymbol{z_s}$	Complex Rotor and Stator Solutions Satisfying IC's at t=0	in (m)
$\boldsymbol{\alpha_{11}}$, $\boldsymbol{\beta_{11}}$	Complex Rotor and Stator Receptances,	in/lb (m/N)
	$\alpha_{11}\left(-\Omega\right)=\frac{1}{k_r-m_r\Omega^2-j\,c_r\Omega}$	
$\delta,\dot{\delta}$	Normal Contact Displacement and Velocity	in, in/s (m, m/s)
γ	Angle Between Clearance Vector x-axis	rad
γ_o	Angle Between Imbalance Vector and Clearance Vector	rad
μ	Friction Coefficient which Satisfies Whirl	-
μ_d	Available Coulomb Friction Coefficient	-
Ω	Rotor Precession Frequency	rad/sec
ω	Rotor Speed	rad/sec
$\omega_{n,comb}$	Combined Natural Frequency of the Rotor-Stator System	rad/sec
ϕ	Traction Angle at Contact Location	-
ξ	Angle Between Clearance and Imbalance Vector	rad

REFERENCES

1. Rosenblum, V. I., 1995, "Entstehung mehrfacher Wellenbrüche nach dem Bruch einer Laufschaufel oder Radscheibe bei Dampfturbinen," Allianz Report, **68**(5), pp. 176–179.

2. Newkirk, B. L., 1926, "Shaft Rubbing," Mech. Eng., **48**, pp. 830–832.

3. Baker, J. G., 1933, "Self-induced Vibration," ASME J. Appl. Mechs., **1**, pp. 5–12.

4. Den Hartog, J. P., 1956, *Mechanical Vibrations*, 4th edition, McGraw-Hill, New York.

5. Johnson, D. C., 1962, "Synchronous Whirl of a Vertical Shaft Having Clearance in One Bearing," J. Mech. Eng. Sci., **4**(1), pp. 85–93.

6. Billett, R.A., 1965, "Shaft Whirl Induced by Dry Friction," The Engineer, **29**, pp. 713–714.

7. Black, H. F., 1967, "Synchronous Whirling of a Shaft Within a Radially Flexible Annulus Having Small Radial Clearance," *Proc. IMechE*, Paper No. 4, **181**, pp. 65–73.

8. Black, H. F., 1968, "Interaction of a Whirling Rotor with a Vibrating Stator across a Clearance Annulus," J. Mech. Eng. Sci., **10**(1), pp. 1–12.

9. Ehrich, F. F., 1969, "The Dynamic Stability of Rotor/Stator Radial Rubs in Rotating Machinery," ASME J. Eng. Ind., **91**, pp. 1025–1028.

10. Choy, F.K., Padovan, J, 1987, "Non-Linear Transient Analysis of Rotor-Casing Rub Events," J. Sound Vib., **113**(3), pp. 529–545.

11. Zhang, W., 1988, "Dynamic Instability of Multi-Degree-of-Freedom Flexible Rotor Systems due to Full Annular Rub," *Proc. IMechE*, Paper No. **C252**(88), pp. 305–308.

12. Lingener, A., 1990, "Experimental Investigation of Reverse Whirl of a Flexible Rotor," *Trans. IFToMM 3rd Intl. Conf. on Rotordynamics*, Lyon, France, pp. 13–18.

13. Crandall, S., 1990, "From Whirl to Whip in Rotordynamics," *Trans. IFToMM 3rd Intl. Conf. on Rotordynamics,* Lyon, France, pp. 19–26.

14. Choi Y.S., 2002, "Investigation on the Whirling Motion of Full Annular Rub," J. Sound Vib., **258**(1), pp. 191–198.

15. Dyck, B.J., 2007, “Experimental Study of Dry-Friction Whirl and Whip for a Rotor Supported by and Annular Rub Surface,” NGST Project Report.

16. Ghauri, M.K.K., Fox, C.H.J., and Williams, E.J., 1996, “Transient response and contact due to sudden imbalance in a flexible rotor-casing system with support asymmetry,” *IMechE Conf. Trans.*, Paper No. **C500**(016), pp. 383–394.

17. Fatarella, F., 1999, “On the Dynamics of Reverse Whirl Due to Rotor/Stator Interaction,” Tesi Di Laurea, Imperial College of Science and Medicine, London

18. Bartha, A. R., 1998, “Dry Friction Induced Backward Whirl: Theory and Experiment,” *Proc. of 5th IFToMM Conf. Rotor Dynamics*, Darmstadt, Vieweg Publishers, Braunschweig, pp. 756–767.

19. Bartha, A. R., 2000, “Dry Friction Backward Whirl of Rotors,” *Dissertation ETH No. 13817*, ETH Zurich.

20. Yu, J. J., Goldman, P., and Bently, D., 2000, “Rotor/Seal Experimental and Analytical Study of Full Annular Rub,” *Proc. of ASME IGTI Turboexpo 2000*, ASME, New York, Vol. 2000-GT-389, pp. 1–9.

21. Cole, M. O. T., and Keogh, P. S., 2003, “Asynchronous Periodic Contact Modes for Rotor Vibration within an Annular Clearance,” *Proc. IMechE, Part C: J. Mech. Eng. Sci.*, **217**, pp. 1101–1115.

22. Jensen, J.D., 1991, “Non-linear Rotor dynamics as applied to Oilwell Drillstring Vibrations,” J. Sound Vib., **147**(l), 115–135.

23. Chen, S. L., Golinval, J. C., and Geradin, M., 1994, “Dry Friction Induced Steady State Backward Whirling Vibration of Rotating Drillstring,” Eur. J. Mech. Eng. M, **39**(3), pp. 157–160.

24. Fumagalli M.A., 1997, “Modelling and Measurement Analysis of the Contact Interaction between a High Speed Rotor and its Stator,” *Dissertation ETH No. 12509*, ETH Zurich.

25. Hunt, K. H., and Crossley, F. R., 1975, “Coefficient of Restitution Interpreted as Damping in Vibroimpact,” ASME J. Appl. Mech., **42**, pp. 440.

26. Childs, D. W., and Bhattacharya, A., 2007, “Prediction of Dry-Friction Whirl and Whip between a Rotor and a Stator,” ASME J. Vib. Acoust., **129**, pp. 355–362.

27. Popprath, S., and Ecker, S., 2007, “Nonlinear Dynamics of a Rotor Contacting an Elastically Suspended Stator,” J. Sound Vib., **308**, pp. 767–784.

28. Williams, R. J., 2004, “Parametric Characterization of Rub Induced Whirl Instability Using an Instrumented Rotordynamics Test Rig,” *IMechE Conf. Trans.*, **C623**(012), pp. 651–660.

29. Williams, R. J., 2004, “A Study of Amplitude Jump Effects in Rotating Systems with Rubs Subjected to Synchronous Excitation,” Technical Report, Rolls-Royce plc, Derby, UK.

30. Neilson, R. D., and Barr, A. D. S., 1988, “Dynamics of a rigid rotor mounted on discontinuously non-linear elastic supports,” *Proc. IMechE, Part C: J. Mech. Eng. Sci.*, **202**(C5), pp.369–376.

31. Tamura, K., Shiraki, K., Awa, K. and Watanabe, Y., 2002, “Vibration Behavior of Rotating Shaft due to Contact with Casing,” *Proc. of 6th Int. Conf. on Mot. and Vib. Cont.*, Urawa, Japan, pp. 1021–1026.

32. Keogh, P. S., and Cole, M. O. T., 2003, “Rotor Vibration with Auxiliary Bearing Contact in Magnetic Bearing Systems, Part I: Synchronous Dynamics,” *Proc. IMechE, Part C: J. Mech. Eng. Sci.*, **217**, pp. 377–392.

33. Grabowski, R., Chapman, L., Crease, G., Friant, J., Gualtieri, G., Kmiec, T., Kincaid, K., Rodriguez, J., 2000, “Testing of an Advanced Liquid Hydrogen Turbopump,” 36th AIAA/ASME/SAE/ASEE Joint Propulsion Conference and Exhibit, Huntsville, AL, AIAA-2000-3678.

34. Childs, D. W., 2004, “Draft: Dry-Friction Whirl/Whip and Pneumatic Hammer,” Private Correspondence.

35. Lu, X., and Khonsari, M. M., 2007 “An Experimental Study of Grease-Lubricated Journal Bearings Undergoing Oscillatory Motion,” J.Trib **129**(3), pp. 640–646.

36. Bijak-Zochowski, M., and Marek, P., 1997, “Residual Stress in Some Elasto-Plastic Problems of Rolling Contact with Friction,” Int. J. Mech. Sci. **39**(1), pp. 15–32,

37. SKF Precision Technologies, 2006, “Integral Motor Spindle Operating Manual,” SKF Precision Technologies, Grafton, Wisconsin.

38. GamGear, 2007, “Economy Series,” <http://www.gamweb.com/view_doc.asp?file=econ_series. pdf>.

39. GamGear, 2007, “EKM Series,” <http://www.gamweb.com/pdf/ekm_series.pdf>.

40. Pavelek, D.E., 2006, “Development of a Test Apparatus for Validating Predictions of (i) Dry-Friction Whirl/Whip and (ii) Transient Hybrid Bearing Performance,” NGST Project Report.

41. Nelson, H.D., 1980, "A finite rotating shaft element using Timoshenko beam theory," ASME J. Mech. Eng. **102**(4), pp. 793–803.

42. Childs, D., 1993, *Turbomachinery Rotordynamics: Phenomena, Modeling, and Analysis*, John Wiley and Sons, New York, pp. 395–431, Chap 7.

43. TAMU Turbomachinery Laboratory, 2002, "XLTRC^2 Brochure."

44. Beatty, R. F., 1985, "Differentiating rotor response due to radial rubbing," ASME J. Vibr. Acoust. Stress Rel. Des., **107**, pp. 151–160.

APPENDIX A

CROSS-REFERENCE CHART

	GENRA				WHIRL					FOCUS				ANALYSIS				MODEL				CONTACT					RUB LOCATION						EXCITATION				EXPERIMENTAL SETUP				
SHORT REF	**APPLICATION**	**ANAL (A)**	**NUM (N)**	**EXP (E)**	**CONTINUOUS (C)**	**PERIODIC (P)**	**SYNCHRONOUS (S)**	**BACKWARD (B)**	**FRACTIONAL (F)**	**STEADY STATE (S)**	**DIAGNOSIS (D)**	**PREVENTION (P)**	**INITIATION (I)**	**LINEAR (L)**	**PARAMETRIC (P)**	**NONLINEAR (N)**	**STABILITY (Y/N)**	**ROTOR (K C M)**	**STATOR (K C M)**	**SYMMETRIC (S)**	**ASYMMETRIC (A)**	**INFINITE (I)**	**LINEAR (L)**	**NONLINEAR (N)**	**ROTOR MATERIAL**	**STATOR MATERIAL**	**DISK (D)**	**SEAL (S)**	**BEARING (B)**	**ROTOR (R)**	**CENTRAL (C)**	**OVERHUNG (O)**	**IMBALANCE (I)**	**DROPPED (D)**	**AMB (A)**	**STRUCK (S)**	**DRIVEN (Y/N)**	**R/C$_R$**	**ROTOR RADIUS (IN)**	**ROTOR ω_{n1} ($^{RAD}/_{SEC}$)**	**STATOR ω_{n1} ($^{RAD}/_{SEC}$)**
1956, Den Hartog, J.P.	TEXTBOOK																																								
1962, Johnson, D. C.	DEAD BAND	A			C		S			S							Y			S									B			O									
1965, Billett, R.A.	DRY FRICTION	A		E	C			B		S				L			Y	KCM	∞	S		∞							B		C					S	Y				
1967, Black, H. F.	SUPERWHIRL	A		E	C		S			S		P		L			Y	KCM	K	S		∞								R	C					S	Y				
1968, Black, H. F.	DRY FRICTION	A		E	C			B		S		P		L			Y	KCM	KCM	S		∞			S	B				R	C					S	Y	6.25			
1969, Ehrich, F. F.	DRY FRICTION	A		E	C			B				P		L			Y	KCM	KCM	S		∞					D					O				S	Y	480	4.8	19	14-25
1974, Begg, I.C.	DRY FRICTION	A			C			B		S		P		L			Y	KCM	∞	S		∞					D					O									
1975, Hunt, K. H., et al.																																									
1979, Childs, D. W.	RUB	A				P	S		F						P					S																					
1985, Beatty, R. F.	RUB	A		E		P			F		D									S																					
1989, Muszynska, A.																																									
1987, Choy, F.K., et al.	RUB	A	N			P		B					I		P	N		KCM	KC	S		∞								R	C										
1988, Zhang, W.	DRY FRICTION	A			C			B		S			I			N	Y	MDF	∞			∞					D					O									
1990, Choy, F.K., et al.																																									
1990, Crandall, S.	DRY FRICTION	A			C			B		S				L			Y	KCM	KCM	S		∞								R	C					S	Y	2-4			
1990, Lingener, A.	DRY FRICTION	A		E	C			B		S				L				KCM	KCM	S		∞								R	C					S	Y	2-4			
1991, Jensen, J.D.	DRILLING	A	N		C		S	B		S				L								∞																			
1993, Childs, D.																																									
1994, Chen, S. L., et al.	DRILLING		N	E	C			B		S				L						S		∞																			
1994, Choi, S. K., et al.																																									
1996, Ghauri, M.K.K., et al.	DRY FRICTION		N	E		P	F	B		T						N					A		L				D					O	I				Y				
1997, Fumagalli M.A.	AMB RETAINER		N	E	C			B				P	I			N		MFD	MDF	S				KC	S	V				R		O		D			N	78.3	0.93		
1999, Fatarella, F.	DRY FRICTION		N	E	C			B		S				L				KCM	KCM	S					A	A	D				C		I				N				
1998, Bartha, A. R.	DRY FRICTION	A	N	E	C	P		B					I			N	Y	KCM	KCM	S				KC	S		D	S			C		I		A		N	1000	7.87		
1998, Chu, F., et al.	RUB	A	N			P	S		F	S			I			N	Y	KCM	∞	S			K				D														
2000, Adams, M. L., et al.	IMPACT			E																																					
2000, Bartha, A. R.	DRY FRICTION	A	N	E	C	P		B					I			N	Y	KCM	KCM	S				KC	S		D	S			C		I		A		N	1000	7.87		
2000, Jiang, J., et al.	DRY FRICTION	A	N		C			B		S				L			Y	KCM	∞	S			K				D				C										
2000, Yu, J. J., et al.	DRY FRICTION	A		E	C			B		S																				R	C		I				Y	40	0.2		
2001, Jiang, J., et al.	DRY FRICTION	A	N		C			B		S				L			Y	KCM	∞	S			K				D				C										
2002, Bently, D. E., et al.																																									
2003, Colakoglu, M.	ROTOR DAMP.																																								
2003, Cole, M. O. T., et al.	BOUNCING	A				P			F	S						N	Y	MDF	KCM	S			KC				D					O	I								
2003, Keogh, P. S., et al.	BOUNCING	A		E		P	S	B	F	S						N		KCM		S			KC																		
2004, Williams, R. J.	DRY WHIRL	A	N	E	C			B		S					P			KCM	KCM	S							D								A					24	109
2004, Williams, R. J.																																									
2005, Choi Y.S.	DRY WHIRL		N	E	C			B		S				L				KCM	KCM	S		I			A	V											Y	9	0.16	145	477.5
2007, Childs, D. W., et al.	DRY WHIRL	A	N		C			B		S				L				MFD	MDF	S		I																			
2007, Popprath, S., et al.	DRY WHIRL	A	N			P		B		T					P	N		KCM	KCM	S			KC																		

APPENDIX B

TEST CASE MATRIX

	File			Score (of 10)			Speed Range			Time				Measured Diameter		Predicted R/Cr		Observed WFR		R/Cr Error %	
	Brg	Case	Length (s)	Up	Dn	SS	Low	High	Low	D	H	M	Delay	D_{BI} in	D_{BF} in	Up Hz	Dn Hz	Up	Dn	Up	Dn
Good Test Cases	B1	12	51	6	6		25	237.5	15	2	2	21		1.5026	1.5027	517	500	647	741	79.93%	67.46%
	B1	18	45			8	25	242.5	22.5	3	5	37	14	1.5027	1.5029	500	469				
	B1	19	60			8	15	240	32.5	3	5	39	2	1.5029	1.5034	469	405		592		68.47%
	L1	14	48	8			20	237.5	0	2	3	12		1.5058	1.5060	246	238	274.3		89.63%	
	L1	15	48	8			25	237.5	0	2	3	25	13	1.5060	1.5068	238	211	267		89.16%	
	L1	16	54		8		0	237.5	15	2	3	54	29	1.5068	1.5069	211	208		238		87.52%
	L1	20	30		10		0	242.5	15	3	5	4		1.5060	1.5060	238	238		254		93.72%
	L1	21	36	10	8		25	240	45	3	5	6	2	1.5060	1.5060	238	238	263.7	247	90.27%	96.38%
	S1	1	132		7.5		0	132.5	15	1	2	13		1.5026	1.5026	517	517		580		89.16%
	S1	2	93	8	6		15	142.5	20	1	2	46	33	1.5026	1.5026	517	517	598	607.4	86.48%	85.14%
	S1	3	60	4	6		15	147.5	15	1	3	14	28	1.5026	1.5026	517	517	556	739	93.01%	69.98%
	S1	4	99	8	7		15	147.5	15	1	3	16	2	1.5026	1.5026	517	517	639.4	615.4	80.88%	84.03%
	S1	5	96		8		0	147.5	15	1	3	19	3	1.5026	1.5026	517	517		634.9		81.45%
	S1	6	123		4		0	237.5	15	1	3	22	3	1.5026	1.5026	517	517		688		75.17%
	S1	7	132		4		35	237.5	15	2	12	29		1.5030	1.5030	454	454	506	552	89.81%	82.33%
	S1	9	60	8.5	8.5		15	237.5	15	2	12	50	11	1.5030	1.5030	454	454	431	755	105.44%	60.19%
	S1	13	48	7	8		32.5	237.5	25	2	1	46	19	1.5036	1.5036	385	385	472	445	81.47%	86.41%
	S1	25	63		6		0	242.5	32.5	3	6	55		1.5036	1.5036	385	385		434.4		88.52%
	S1	26	96	6			15	242.5	0	3	6	57	2	1.5036	1.5036	385	385	444.7		86.47%	
	S2	22	54			7	0	242.5	22.5	3	5	55		1.5026	1.5026	517	517		570		90.73%
Bad Test Cases	B1	17	21				20	222.5	0	3	5	23		1.5027	1.5027	500	500				
	S1	8	15				0	0	0	2	12	39	10	1.5030	1.5030	454	454				
	S1	10	267				0	0	0	2	1	5	15	1.5030	1.5036	454	385				
	S1	11	36				0	0	0	2	1	27	22	1.5036	1.5036	385	385				
	S2	23	69				0	0	0	3	6	14	19	1.5026	1.5026	517	517				
	S2	24	141				0	0	0	3	6	29	15	1.5026	1.5026	517	517				
	T1	27	51				0	0	0	4	1	29		1.5022		600					
	T1	28	117				0	0	0	4	2	40		1.5040		349					

S1=Small Rub 1
S2=Small Rub 2
L1=Large Rub 1
B1=Babbit Rub 1
T1=Steel Rub 1

VITA

Name: Jason Christopher Wilkes

Address: Texas A&M Turbomachinery Laboratory
Texas A&M University, Mail Stop 3123
College Station, TX 77843-3123

Email: jasonwilkes@tamu.edu

Education: M.S., Mechanical Engineering, Texas A&M University, August 2008.
B.S., Mechanical Engineering, Texas A&M University, August 2005.

Interests: Rotordynamics of turbomachinery: phenomena, modeling, and analysis.